

Durham Research Online

Deposited in DRO:

09 October 2020

Version of attached file:

Accepted Version

Peer-review status of attached file:

Peer-reviewed

Citation for published item:

Pastoriza-Primaleon, Loraine and McCaffrey, Kenneth J.W. and Holdsworth, Robert E. (2020) 'Fracture attribute and topology characteristics of a geothermal reservoir : Southern Negros, Philippines.', *Journal of the Geological Society.*, 177 (5). pp. 1092-1106.

Further information on publisher's website:

<https://doi.org/10.1144/jgs2019-126>

Publisher's copyright statement:

Pastoriza-Primaleon, Loraine, McCaffrey, Kenneth J.W. Holdsworth, Robert E. (2020). Fracture Attribute and Topology Characteristics of a Geothermal Reservoir: Southern Negros, Philippines. *Journal of the Geological Society* 5: 1092-1106 <https://doi.org/10.1144/jgs2019-126> © Geological Society of London 2020.

Use policy

The full-text may be used and/or reproduced, and given to third parties in any format or medium, without prior permission or charge, for personal research or study, educational, or not-for-profit purposes provided that:

- a full bibliographic reference is made to the original source
- a [link](#) is made to the metadata record in DRO
- the full-text is not changed in any way

The full-text must not be sold in any format or medium without the formal permission of the copyright holders.

Please consult the [full DRO policy](#) for further details.

FRACTURE ATTRIBUTE AND TOPOLOGY CHARACTERISTICS OF A GEOTHERMAL RESERVOIR: SOUTHERN NEGROS, PHILIPPINES

Loraine Pastoriza Primaleon^{*1,2}, Kenneth J.W. McCaffrey¹, and Robert E. Holdsworth¹

¹Department of Earth Sciences, Durham University, Durham, DH3 1LE, United Kingdom

²Subsurface Group - Geothermal Resource, Energy Development Corporation, Ortigas, Pasig City,
1605 Philippines

*Correspondence (pastoriza.lr@energy.com.ph)

Running header – Fracture attributes and topology of a geothermal reservoir

Supplementary material: Slopes, coefficient of determination, and AIC values of the cumulative
frequency versus length and aperture plots of all fracture transects is available

ABSTRACT

The characterization of fracture networks using attribute and topology analyses has not been widely applied to geothermal resources in order to better understand and predict secondary porosity, permeability, and fluid flow characteristics. In this study, fracture length, aperture, intensity, and topology data were acquired from remotely sensed images and surface exposures from the Cuernos de Negros region, and compared with well cores and thin sections from the underlying active geothermal reservoir: the Southern Negros Geothermal Field (SNGF), west central Philippines. We show that the fracture attributes for the analogue and reservoir are best described by a power law distribution of fracture length and aperture intensity across six to eight orders of magnitude. This characterization of outcrop and borehole fractures validates the use of surface exposures as analogues for the SNGF reservoir rocks at depth. An observed change in the scaling exponent in the 100 to 500 m length-scales suggests that regional to sub-regional fracture systems scale differently to those at the mesoscale and macroscale, which may be a strata-bound effect or a sampling issue. Topology analyses show a dominance of Y-nodes and doubly connected branches, which indicates a high degree of fracture connectivity that is important for effective fluid flow.

Fracture attribute analysis is a key tool used in the characterization and modelling of fracture networks in fracture-dominated reservoirs. We use the term ‘fractures’ here in a general sense to include features such as faults, joints, and veins. Fracture analysis involves creation of an understanding of the size, spatial characteristics, and scaling of physical fracture attributes such as intensity (spacing), length, aperture and connectivity, all of which may control fluid flow (e.g. Zeeb *et al.* 2013). Throughout this paper, the term ‘fracture scaling’ is used to refer to the relationship of fracture system properties at one observational scale to those at another scale, as defined in Bonnet *et al.* (2001). To obtain a realistic and accurate fracture scaling model, data should ideally be collected from the reservoir itself, but in most cases where availability of geophysical data, borehole images and well cores is limited, the use of analogue surface datasets is widely adopted (e.g. Guerriero *et al.* 2010; Mäkel 2007; Antonelli *et al.* 1999; and many others). Additionally, collecting fracture data from boreholes can have its own disadvantages: sampling of fractures is strongly controlled by borehole orientation and inclination; length is difficult to directly measure; and large fractures are rarely sampled (see Ortega *et al.* 2006; Zeeb *et al.* 2013).

In hydrocarbon systems, the use of surface analogues in fracture attribute analysis to visualize the reservoir rocks is common (e.g. Watkins *et al.* 2015; Pless 2012; Wennberg *et al.* 2007). However, in geothermal systems, especially those hosted in dominantly crystalline rock-hosted reservoirs where the understanding of fracture network is similarly critical, the number of published studies that have used a fracture attribute characterization approach is still low, although some pioneering examples have been published (e.g. Weydt *et al.* 2018; Bauer *et al.* 2017; Bar *et al.* 2011; Chesnaux *et al.* 2009). Fractal (power law scaling) fracture distributions have been documented within crystalline geothermal systems for fracture lengths (Watanabe and Takahashi 1995) and aperture (Barton and Zoback 1992; Ledéseret *et al.* 1993). Recent work by Massiot *et al.* (2015) analyzed fracture width - which they defined as the fracture-normal distance between walls (equivalent to the kinematic aperture of Ortega *et al.* 2006) - and the spacing of borehole fractures in the Rotokawa Geothermal Field in New Zealand. They found that fracture widths are best described by an exponential distribution whilst spacing is better represented by a log-normal, power-exponential or gamma distribution. These published studies were necessarily limited to the scale of individual boreholes. By contrast, the aim of this study is to provide one of the first *multiscale characterizations* of a geothermal system using a range of surface and subsurface datasets.

In this paper, the fracture network in the Southern Negros Geothermal Field (SNGF) is characterized in the west Central Philippines, using five datasets covering eight orders of magnitude scale – thin sections, rock slabs, well cores, outcrops, and lineament maps. A primary aim of this analysis is to evaluate whether the readily accessible fracture datasets seen at the surface in Negros (e.g. from outcrops and satellite images) are good quantitative analogues for the fracture networks in the geothermal reservoir rocks at depth. The ultimate objective here is to identify the statistical

behaviours of the fracture sizes and spacing and to determine the topological properties within the SNGF fracture system. These fracture properties have important and direct implications for the fracture connectivity and permeability of the geothermal network in the subsurface.

GEOLOGY OF THE AREA

The SNGF is an actively producing liquid-dominated geothermal resource with a presently installed capacity of 218 megawatts. It is hosted by the andesitic Cuernos de Negros volcanic complex in the southern tip of Negros Island in the Central Philippines (Figure 1a). The host volcano is part of a 260 km long chain of Quaternary volcanoes related to active eastward subduction along the Negros Trench. Deep drilling to 3300 m depth over the last three decades reveals that the Cuernos de Negros volcanic complex was created by several volcanic and intrusive events. The oldest rocks drilled are ca 990 m thick, Miocene altered andesites intercalated with tuffs and calcarenites with occasional volcanic and sedimentary breccias (Puhagan Volcaniclastic Formation, Figure 1c). These rocks are cross cut by the Nasuji quartz monzodiorite to micromonzodiorite pluton which led to the formation of a metamorphic aureole known locally as the Contact Metamorphic Zone. Geochronological studies of the pluton have yielded contradicting ages (Miocene ca 10.5 Ma using K-Ar in Ariceto-Villarosa *et al.* 1988 and Zaide 1984 versus Pleistocene ca 0.7 to 0.3 Mya using Ar-Ar in Rae *et al.* 2004). By the Early Pliocene, the Okoy Sedimentary Formation, followed by the overlying undifferentiated andesitic volcanics and pyroclastic rocks of the Southern Negros Formation were deposited. All of these rocks are intruded by at least two suites of dykes during the Pliocene (Figure 1c). The youngest Quaternary-aged andesitic Cuernos Volcanics are subdivided into different members depending on which volcanic edifice of the Cuernos de Negros (CDN) volcanic complex they are associated with. Radiocarbon dating of charred wood suggests a youngest eruption age of 14,450 years (Zaide 1984). These young volcanic rocks cover much of the surface of the present-day CDN volcanic complex, with exposures of the older Southern Negros Formation limited to the downstream river valley area of the E-W Okoy River (Figure 1b). The Pliocene sedimentary and volcanic sequences and older intrusive bodies presently host the active geothermal field that is believed to be heated by the younger intrusive system.

All of the volcanic rocks are affected by brittle deformation which can be separated into two groups, Group 1 and Group 2, based on fault rock characteristics, associated alteration type, and kinematics, as detailed in Pastoriza (2017) and Pastoriza *et al.* (2018) and summarized in Table 1. Based on crosscutting relationships, these two groups of fractures developed during at least two fracturing events with the Group 1 features developing during Stage 1 (likely during the Pliocene), and the Group 2 fractures during Stage 2a and Stage 2b (which occurred during Pleistocene to Recent times), with Stage 2b mostly related to reactivation of both Group 1 and Group 2 fractures (Pastoriza *et al.* 2018).

Stress inversion analysis of slickenlines along faults associated with each of the three stages of crosscutting features gives an indication of the prevalent stress regime associated with each deformation event over time (Figure 2; Pastoriza *et al.* 2018). Stage 1 occurred under a strike-slip to transpressive tectonic regime (σ_1 horizontal) changing to an extensional setting during Stage 2 (σ_1 vertical). The minimum principal direction, σ_3 , was oriented E-W for Stage 2a then rotated to a more NE-SW orientation during Stage 2b (Figure 2).

The present stress regime of Negros is characterized by a general WNW-ESE to NW-SE-oriented horizontal compression (Lin and Lo, 2013; Rangin 2016; Rangin *et al.* 1999) consistent with the tectonic setting of the Philippine archipelago. The last destructive earthquake on Negros Island was a M_w 6.7 in February 2012 located in the central coast area (USGS 2012), generated by the NNE-SSW-trending NW-dipping Yupisan Fault (Aurelio *et al.* 2017; Figure 1a). This structure runs to the west of the Cuernos de Negros Volcano, and together with the Pamplona Anticline in southern Negros, forms part of a fold-thrust system presently active on the island (Aurelio *et al.* 2017; Pastoriza 2017). This implies a consistent WNW-ESE compressional tectonic regime, similar to the stress configuration recognized during Stage 2b. It has been further suggested that propagation of the Yupisan Fault has influenced the local rotation of stresses observed in the SNGF (Pastoriza *et al.* 2018).

Permeability within the SNGF is known to originate mostly from fractures and less from intraformational sources based on borehole drilling and geological indicators. Radial calculations carried out in Pastoriza (2017) using actual permeability measurements of intact reservoir rocks and measured well flow rates in some SNGF boreholes show that matrix permeability contributes no more than 1% of the measured injectivity rates. As discussed by Pastoriza *et al.* (2018), the SNGF reservoir development is most likely related to the Group 2 fractures based on the nature of the alteration and their intimate association with active and recently active thermal manifestations. Pastoriza *et al.* (2018) showed that the Group 2 fractures comprise kinematically-compatible shear and opening-mode fractures (hybrid and tensile), which contain the same fills and characteristic alteration assemblages (Table 1). These authors also performed a slip and dilational tendency analysis to show that the Group 2 structures were most likely to be the ones associated with the geothermal system. The present hydrological model of the SNGF (Bayon and Ogena 2005) indicates two outflow directions for the geothermal field, one towards the northeast, and another to the northwest. Well measurements suggest that permeability is higher in the northwestern direction, where the Nasuji Pluton is known to be located in the subsurface. Group 2 fractures associated with extensive alteration of their host rocks are well exposed in this part of the SNGF. Thus, the importance of understanding the size, spatial distribution and connectivity of Group 2 fracture networks within the SNGF is the motivation for this study.

FRACTURE SIZE ANALYSIS

Many studies have shown that fracture attributes (length and aperture) of natural fracture systems are commonly described by power law distributions (e.g. Hooker *et al.* 2014; Ortega *et al.* 2006; Marrett *et al.* 1999; McCaffrey and Johnston 1996; Walsh *et al.* 1991; Scholz 1987). In some circumstances, attributes may also be described by *log-normal*, *exponential*, and *gamma law* (Bonnet *et al.* 2001). Normal and log-normal distributions usually provide a good description for fracture systems with characteristic lengths (Hooker *et al.* 2014; Bonnet *et al.* 2001). This is usually true when fracturing is significantly controlled by lithological layering, e.g. strata-bound jointing (Odling *et al.* 1999; Gross *et al.* 1997). Exponential law distributions also incorporate a characteristic scale, e.g. a mean or a modal value (Bonnet *et al.* 2001), but are typical of more random distributions (Gillespie *et al.* 1993). As mentioned in Hooker *et al.* (2014), an exponential distribution may return a negative fracture size at certain frequencies which suggests that the distribution is not scale-independent. Lastly, gamma law distributions are common in earthquake statistics (Bonnet *et al.* 2001) and exist in the form of a power law with an exponential tail at smaller sizes.

Methods

Collection of fracture data was performed both in 1D using linear transects and in 2D circular scanlines and windows. Linear scanlines are most subject to bias (see Watkins *et al.* 2015; Zeeb *et al.* 2013). However, the heavy jungle vegetation in the region leads to scanline length limitations and fractures with low intersections relative to the angle of the transect line. Thus it was for many exposures in this study area the most practical and convenient method for collecting data. Linear scanlines (transects) can be used easily at all scales of observation and on different types of datasets. Carrying out a circular scanline, where possible, allows the issue of bias to be addressed, although it provides a more limited range of attribute data (i.e. number of fracture intersections and endpoints).

For easier reference in the text, transects in which the structures on the digital elevation models are sampled at 1:500,000 and 1:250,000 scales covering the entire Negros Island are referred to as *regional* transects, whilst those sampled at 1:100,000, 1:50,000, and 1:20,000 encompassing the SNGF are termed *sub-regional* transects. Outcrop transects are referred to as *macroscale* transects, well cores – *mesoscale*, and thin section datasets – *microscale*.

The fracture size analysis reported here involves the collection and evaluation of the distribution of the fracture length and (kinematic) aperture in 1D over three scales – regional, macroscale, and mesoscale (Figure 3). Thin section and rock slab samples were not included in the 1D sampling as it was difficult to find areas on samples that are cut by sufficient numbers of fractures for analysis. Regional fractures are geologically controlled topographic lineaments manually picked using a 90-m Shuttle Radar Topography Mission (SRTM) data (Jarvis *et al.* 2008) and 10-m TerraSAR-X digital elevation models. These were carried out at 1:500,000 and 1:250,000 scales for the SRTM data, and

1:100,000, 1:50,000, and 1:20,000 scales for the TerraSAR-X dataset. To minimize any potential orientation bias and to enable the maximum number of fractures to be collected, four transect lines were used on each lineament map. These are oriented 0° (N-S), 045° (NE-SW), 090° (E-W), and 315° (NW-SE, Figure 3a). It was decided that each transect line should cross, at least in part, the region of the volcano (for 500K and 250K scales) and the Okoy Valley (for 100K, 50K, and 20K scales). As noted by Pastoriza *et al.* (2018), the most prominent lineaments are an ENE-WSW-trending set that coincide with the Okoy River. They appear to be discontinuous and arranged as right-stepping en-echelon features, representing the mapped traces of the Puhagan Fault Zone (Figure 1b). Geomorphological kinematic indicators such as push-up ridges observed along the trace of this fault zone suggest that it has a dextral sense of movement.

Outcrop 1D (macroscale) transects were mostly conducted within the boundaries of the SNGF, where exposures were large enough that a long measuring tape (30-50 m) could be used (Figure 3c). A perpendicular transect line to the main fracture set is ideal to get the true spacing of the fractures. Where this was not possible because of outcrop limitations or because there are no clear dominant fracture sets present due to there being mutually crosscutting fractures, the transect line orientation was dictated by the outcrop dimensions to enable the intersection of as many fractures as possible. Accessibility and exposure of fractured rocks permitting at least 225 fractures were sampled at each site as suggested by Zeeb *et al.* (2013) in order to adequately capture the statistical properties of the studied fracture network. Linear transects in well cores were performed in a similar manner except that since the well cores are not oriented, only a relative orientation with respect to the transect line can be measured (angle measured down from the horizontal in a clockwise direction, Figure 3d). Transect lines were mainly laid out parallel to the length of the core. The curved surface of the core is treated as a flat face, which limits the length of fractures, when they are measured.

For each fracture intersected by the transect line, where applicable, the distance from the start of the transect, fracture type, orientation, length, kinematic aperture, infill type, termination type, and observed cross-cutting relationship were recorded. The kinematic aperture for opening mode or hybrid fractures (Ortega *et al.* 2006) is equivalent to the fracture width, measured perpendicularly between the fracture walls using a ruler or a feeler gauge, *including* any fill. Of these attributes, length and aperture were best sampled and the following analysis focuses on these attributes. Note, however, that fractures for each sampling scale were analysed altogether (i.e. they were not divided further by orientation or by type). This was necessary due to limitations in our available sample sizes, meaning that further subdivision of the fractures was not statistically appropriate.

Fracture size distributions are represented using cumulative frequency plots following the procedure detailed in Ortega *et al.* (2006). Model selection was based on the resulting value of determination, R^2 from the ordinary least squares regression, and the Aikake Information Criterion (AIC) which is a

maximum likelihood estimator, which is calculated in the **R** statistical package. Clauset *et al.* (2009) suggested that the maximum likelihood estimation (MLE) method is more appropriate for describing power law relationships in empirical data rather than ordinary least squares (OLS) regression techniques. This is based on the observation that in linear regression, standard errors are poorly constrained and so that such regressions are not valid tests for probability distributions. Further, these authors suggested that R^2 provides little information to be able to validate a power law fit effectively. Here, we report the MLE scaling exponents (following Rizzo *et al.* 2017 and Clark *et al.* 1999) and the AIC is calculated to determine the quality of fit.

The coefficient of variation, C_v , defined as the standard deviation divided by the mean of the fracture spacing, is also reported here to describe the degree of clustering of fractures within a sample line. Where the C_v is >1 , it is suggested that the fractures are clustered, whilst they are regularly-spaced if C_v is <1 (Gillespie *et al.* 1999). If C_v is ≈ 1 , the fractures are randomly-spaced (Mäkel 2007).

Sanderson and Nixon (2015) use topology to describe the spatial relationships between geometrical features within a fracture network, encompassing how fractures interact with each other; thus this approach evaluates the connectivity and continuity of the fracture system. In two dimensions, a fracture array consists of *lines*, *nodes*, and *branches* (Figure 3e). Nodes are where fractures intersect or terminate, whilst two nodes bound a branch. An entire length of a fracture may be formed by a series of nodes and branches. Nodes may be described as *isolated* (*I-node*), *crossing* (*X-node*), or *abutting* or *splaying* (*Y-node* or *T-node*) (Figure 3e; Sanderson and Nixon 2015; Manzocchi 2002). Good connectivity in a fracture system suggests an abundance of X- and Y-nodes (Manzocchi 2002). Branches, on the other hand, are described based on the node types that occur at either end. Thus they can be an *isolated* (*I-I*), *partly connected* (*I-C*), or *doubly connected* (*C-C*) branch, where a connected node is either a Y or an X-node (Sanderson and Nixon 2015).

The 2D circular sample windows were used for the collection of nodal information on five different scales of datasets: regional lineament maps; outcrops; well cores; slabs; and thin sections. In each transect, number of endpoints and connection types were taken (Figure 3e). Rohrbaugh *et al.* (2002) suggested that the diameter of a circular scanline should be larger than the fracture spacing and smaller than the minimum dimension of the sampling region. They further advised carrying out at least ten scanlines per sampling region and that there should be more than 30 endpoints (*I-node*) delineated in each scanline (Rohrbaugh *et al.* 2002). In this study, all these recommended conditions were met, but some proved to be challenging particularly because of the limited surface exposures and number of clean fractured rock sections. In many instances, the suggested diameter can be easily achieved, but the number of fractures encompassed is usually rather low. To be able to get at least 30 endpoints, a scanline larger than the sampling region was required, which is impossible. It was then

necessary to compromise in designing the scanlines to maximize sampling of the fracture network. All the nodes are then delineated within the circular scanline and are counted thereafter.

The node types are visualized using a ternary diagram. Additionally, from the number of nodes, the number of branches and number of lines can also be calculated following the methods in Sanderson and Nixon (2015). A ratio of the number of lines and the number of branches, N_B/N_L , approaching 1 suggests that the network is I-node-dominated, whilst a value of ≈ 3 is dominated by Y-nodes, and an N_B/N_L approaching infinity is dominated by X-nodes. Using the number of each node type, the probabilities of the branch type, P_{II} , P_{IC} , and P_{CC} , were also derived and represented on a ternary diagram (Sanderson and Nixon 2015). Using the average number of connections per branch, C_B , the level of connectivity of the fracture network can easily be interpreted. C_B ranges between 0 to 2, and where highest, suggests that the network is well connected (dominated by doubly connected branches, where nodes are either X or Y). Sanderson and Nixon (2015) concluded that C_B is a better measure of the connectivity of the fracture than the number of connections per line, C_L .

The topology results presented in this study were assessed with reference to the variation in the host lithology, proximity to major fault zones (macroscale) and proximity to intra-reservoir permeable zones (mesoscale). Identifying whether a fault zone has been intersected in the subsurface requires a combination of indicators that include the geology, drilling parameters, and the results of post-drilling completion tests. The location of the permeable zones within the borehole was used as an indicator of whether a fault exists at a particular depth. Permeable zones are depth intervals within a borehole which can be identified during a spinner survey test as part of the well completion activities. These zones are usually marked by an increase of the fluid velocity as the spinner equipment is lowered whilst pumping fluids at constant rates. Where the fluid velocity increases, it is inferred that the borehole diameter has enlarged, potentially because of the presence of open fractures (related to large-scale faulting) and is feeding fluids into the borehole.

Fracture size results

A total of 40 line sample transects were completed for this study including 20 regional and sub-regional transects across five lineament maps (at four orientations for each scale), eight macroscale transects, five of which are within the SNGF reservation area whilst three are scattered across other parts of Negros Island, and 12 short mesoscale transects (Table 2). Macroscale transects were performed on representative outcrops of Southern Negros Formation and the younger Cuernos Volcanics whilst mesoscale core samples were mostly taken within the intrusive body and two samples from the Southern Negros Formation (Table 2). Ideally, fractures can be sub-divided according to their type and orientation. However, because of the limited number of fractures collected, further reclassification tends to reduce the sample size significantly below levels where the statistical

analyses would be valid. Thus, macroscale and mesoscale samples were grouped and analysed together.

The length of the regional transects ranged from 23×10^3 to 190×10^3 m whilst for the sub-regional set it was 6×10^3 to 21×10^3 m (Table 2). At the outcrop level, the maximum transect length carried out was 35 m whereas mesoscale transects only ranged between 0.08 to 0.34 m long. Since the well cores are fragmented, it was impossible to conduct longer transects.

ENE-WSW-oriented lineaments are predominant, followed by NW-SE and NE-SW trends both at the regional and sub-regional scales (Figure 3b). At the macroscale, fractures striking NW-SE and a subordinate NE-SW set are most abundant, with the NW-SE oriented features being mostly related to the Stage 2 fracture formation episodes (Figure 2; Pastoriza *et al.* 2018).

Fracture intensity versus length

Viewed as individual datasets, ten out of the 12 regional transects and seven out of the eight sub-regional datasets are best described by a log-normal distribution based on the AIC values (see Supplementary Material 1). At the macroscale, AIC values suggest that the fracture distribution could either be a log-normal or a power law. This observation differs from the mesoscale where transects strongly follow a power law distribution. Given that the mesoscale and macroscale datasets can both be described using a power law applying the MLE method, a multiscale plot was created in log-log space (Figure 4) to examine the scaling properties of the structures across eight orders of a magnitude in length scale. The plot reveals a clear break in slope between the mesoscale and macroscale (1×10^{-3} to $\sim 5 \times 10^1$ m) datasets versus the regional and the sub-regional (5×10^2 to 1×10^5 m) fracture populations. This suggests that some kind of change in the scaling properties is present. The fracture length distributions from cores and the outcrops yield a well-constrained distribution with a slope of -0.90 with a calculated coefficient of variability of 0.22 (Figure 4). On the other hand, the mean slope for the regional fracture lengths is steeper at -1.70 with a coefficient of variability of 0.26 (Figure 4). A paucity of fracture data with lengths between 100 to 500 m means that it is difficult to constrain this change point further. Overall, the datasets align well showing that a power law distribution could be a reasonable description across eight orders of magnitude scale albeit with a change in scaling at ca 100 m fracture length.

Fracture intensity versus kinematic aperture

Unlike the cumulative plots of length, which display a range of distributions, the fracture kinematic aperture data from SNGF are all well described by a power law distribution based on the AIC values (refer to Supplementary Material 2). Note that kinematic aperture data are only available at the macroscale and mesoscale. For the transect lines carried out at the macroscale, aperture sizes range from 5.0×10^{-6} to 9.6×10^{-1} m for those within the SNGF, and 1.0×10^{-5} to 6.50 m for those outcrops outside the geothermal field. There are also fractures with no measurable aperture (aperture = 0) in

both groups, where the fracture is closed or too fine to measure. A combined log-log plot of normalized aperture data from the mesoscale and macroscale (Figure 5) indicates the well-constrained nature of the power law distribution of the cumulative frequency with the aperture across five magnitude scales (10^{-2} to 10^3 mm). The exponents which are close to -0.5 to -0.6 for both datasets (macroscale and mesoscale) are quite consistent, although the mesoscale generally displays higher density fracturing (i.e. higher y-axes intercepts). The overall slope average using the MLE method is -0.59 (Figure 5).

Topology results

The database of circular transects comprises 70 individual datasets made up of four regional lineament maps, 13 macroscale surface rock exposures, and 14 mesoscale boreholes (Figure 6). Note that there is only one thin section (microscale) scanline as most thin sections poorly sampled fracture sets in rocks. Diameters of the scanlines range between 5.70×10^{-3} to 2.08×10^4 m covering areas from 2.55×10^{-5} to as much as 5.33×10^8 m². In general, at least up to the outcrop scale, the observed number of nodes appear to increase with the observation scale, where the average number of nodes per scale is lowest for the thin sections (15 nodes), progressively increasing up to the outcrop level (304 nodes on average), with a maximum number of nodes of 900 (Figure 6).

Figure 7a shows a plot of all the node-type proportions for the 70 circular scanlines across all five sampling levels. A general spread of the I/X/Y ratios is observed, but overall, it appears that X-nodes have low abundance in all the examined fracture populations. An exception is the lineament group that has low numbers of Y-nodes. Overall, a significant proportion of the circular scanline results plot close to the Y-node apex, with Y-nodes comprising at least 60%. This concentration is composed of the majority of the outcrop datasets, the three core samples, and two slab scanlines. Most of the core samples, together with a few outcrop data, plot in the central areas of the diagram, where there are roughly equal proportion of X- and Y-nodes and just a slightly higher proportion of the isolated nodes. This ternary diagram is accompanied by the ratio of the number of lines to the number of branches, N_B/N_L (Sanderson and Nixon 2015), indicating that 71% of the entire sampled population has N_B/N_L ratios between two to three (Figure 7b). This shows that the SNGF fracture system is predominantly Y-node-dominated.

The nodal type distributions can be further explored in terms of how they may be influenced by alteration, major fault proximity, and the fracture group they belong to. The type of host rock appears to have little influence on the node type developed, albeit acknowledging the limitation that the macroscale transects were performed on the young lava flows and tuffs exposed at the surface. Figure 8a categorises the samples according to whether the sampled fractures are associated with mineral alteration (red), or not (blue). The majority of the fractures that are not associated with alteration are joints. There is a general increase in observed X-nodes in fracture populations that are associated

with an alteration. Figure 8b classifies the scanlines in terms of how close they are to a major fault. A major fault in this context is any fault with at least a 10 cm width fault core, or that can be traced for at least 5 m. There is a strong relationship between proximity to a major structure and the type of nodes delineated. Scanlines represented as red dots are those where the sample is proximal (within at least 2 m) to a major fault, whilst those in blue do not have observed major faults within 2 m. Clearly, a concentration of red data points is observed close to the Y-node apex whilst blue ones tend to spread away from it and towards the I-node apex (Figure 8b). This distribution suggests some preference for connected fracture populations closer to major faults compared to isolated structures. Lastly, Group 1 fracture populations are distinctly dominated by I-nodes whereas Y-nodes are the most abundant in Group 2 fracture arrays (Figure 8c). The classification into the groups was based on field observations where Group 1 fractures are dominated by pyrite-infills and are consistently older than Group 2 fracture sets (see Pastoriza *et al.* 2018).

The well core topology data were analysed in the context of host rock lithology, depth, associated permeable zones, and fracture types (i.e. Group 1, 2, etc). The host lithology of the sampled well cores can be divided into three types – andesite lavas, intrusive rocks, and clastic rocks. The andesite lavas include a porphyritic facies, the intrusive rocks are associated with the Nasuji Pluton (diorites, hornfels, and associated facies) and younger dykes, whilst tuffs and tuff breccias and a sandstone sample comprise the clastic rocks. As shown in Figure 9a, there is no clear preferential concentration of the rock type with the node type. Andesite samples have either abundant Y-nodes or have relatively abundant I-nodes. Intrusive rocks and the four clastic samples likewise plot in generally different regions of the ternary diagram (Figure 9a).

The well core samples are classified according to whether they were collected at depths where a permeable zone has been identified (Figure 9b). The aim here was to provide a comparison with the identified macroscale trend between fault proximity and abundance of connected branches based on the assumption that permeable zones directly correspond to fault zones. As shown in Figure 9b, the trend where connected fractures are predominant closer to a fault zone is not observed at the well core level. However, we suggest that this result is likely to reflect the inherent resolution difference between the macroscale and the mesoscale since the minimum thickness of permeable zones identified in the wells is 50 m compared to the distance limit of 2 m from major faults in outcrops.

Finally, the circular scanlines were evaluated based on whether the fractures are vein-dominated or not. The intention here is similar to the alteration analysis at the macroscale. Since it is difficult to preserve centimetre-wide fractures with evidence of channelling hydrothermal fluids (core samples tend to break along these kinds of fractures), veins were used as an alternative to indicate the transport of fluids. In general, vein-dominated fracture arrays in the well cores produce a dominance of Y-

nodes (>60%) or an equal proportion of Y- and X-nodes (10 to 40%), but where I-nodes are not as abundant (Figure 9c). Those without veins on the other hand have a general spread of nodal characteristics. Finally, corrected depths, expressed in meters below sea level (mBSL), where the samples were collected was also considered. Unsurprisingly, there is no trend with depth and node type (Figure 9d).

Considering the different branch types for all samples and whether they are isolated, partly connected, or doubly connected, 70% of the fracture populations are dominated by doubly connected fracture branches. Figure 10a shows that a majority of the scanlines plot close to the P_{CC} apex. This is consistent with the calculated C_B values of most outcrops, which range between 1.6 to 2, suggesting high connectivity for the majority of the fracture systems sampled (Figure 10b). The clear exceptions here are the I-node dominated core samples and the outcrop scanlines which sampled Group 1 fractures. Additionally, the topology from the lineament maps plot midway along the curve where C_B is ~ 1.0 which suggests a higher probability for partly-connected fractures to occur within the fracture array (Figure 10a).

DISCUSSION

A key objective in our analysis was to test the assumption that the fracture networks exposed at the surface are good analogues for the fracture arrays in the SNGF reservoir rocks. Macroscale transects were mostly taken across the young Cuernos Volcanics lava flows and tuffs and the Pleistocene Southern Negros Formation outcrops. Cores on the other hand sampled the reservoir rocks – the Pliocene Okoy Sedimentary Formation, the Pleistocene Southern Negros Formation, and the intrusive bodies. Our previous work has shown that the fracture systems associated with the main geothermal system are the Group 2 structures seen in both reservoir samples and outcrops. We comment further on the scaling attributes of both these systems below. It is also worth considering that in areas with a relatively young, still active and overall short deformation history – our Stage 1, Stage 2a, Stage 2b (Pastoriza *et al.* 2018) - it is very likely that the analogue and the reservoir have experienced the same tectonic events. Thus our assertion that there is a clear similarity between the mesoscale and macroscale fracture networks attributes has a sound geological basis.

Another important objective in the fracture analysis was the development of a *multiscale approach*. The fracture attribute and topology analyses carried out here enabled us to visualize the scaling properties and connectivity of the fracture populations covering six (kinematic aperture) to eight (length) orders of magnitude within SNGF. Evaluation over a larger range satisfies the suggestion of Bonnet *et al.* (2001) that it is desirable to define statistical properties over at least three orders of magnitude scale range in order to assess scaling properties. Furthermore, the employment of combined sampling methods in different dimensions enables us to *maximize* the information gathered from limited datasets whilst at the same time, *minimizing* the limitations inherent to each sampling

method. Conducting the 1D transects provided attribute data that are not easily collected in the less spatially biased 2D circular scanlines. This combined approach strengthens the reliability of our characterization of the fracture systems. The results show very clearly that with a larger range, the relationships are either better constrained or that changes of the distribution properties are easier to capture compared to single-scale studies.

In our fracture size distribution evaluation, the MLE method has been incorporated into model selection and scaling parameter estimation. The method is widely used in other disciplines (e.g. biology, psychology, marketing), but its application to fracture attribute analysis is still relatively novel (Massiot *et al.* 2015; Rizzo *et al.* 2017). Adding maximum likelihood estimators such as the AIC strengthens the model selection. Given the superiority of MLE compared to standard least squares regression methods, it seems reasonable to regard the scaling parameter obtained to be more robust (as discussed in Clauset *et al.* 2009 and Clark *et al.* 1999).

The results obtained from the fracture intensity versus size analysis are consistent with many examples previously described in the literature (e.g. Hooker *et al.* 2014; Marrett *et al.* 1999; McCaffrey and Johnston 1996; Ledésert *et al.* 1993) suggesting that many natural fracture networks may be described by a power law distribution (Figure 4, Figure 5). Individually, a number of the datasets are better described by either an exponential or a log-normal model. In the present study, for example, most of the regional fracture length distributions are better described by a log-normal distribution.

It should be noted that the lineaments picked in this study are assumed to be all natural fractures. Ground verification for all of the lineaments could not be carried out routinely in this heavily-vegetated region, and so, the possibility that some of the lineaments are not fracture-related or are man-made structures cannot be completely disregarded. As we discuss, this limitation may have also affected the statistical distribution for the regional and sub-regional length data. Thus, the log-normal distributions observed could be explained by two possibilities.

Firstly, it is well known that power-law distribution datasets that have been degraded by truncation and censoring effects may resemble exponential or log-normal distributions (Pickering *et al.* 1995). The effect of the low resolution of the satellite images biasing the fracture length is likely to be the issue here, limiting the scale range over which lineaments can be picked. A further consideration is that the major fracture systems in Negros are related to known active tectonic structures in the region (e.g. the Yupisan Fault; see Aurelio *et al.* 2017). These large structures will have cut through the layering, so that resulting distributions might not necessarily be scale-bound. Potentially, it is possible that in this study, only large-scale lineaments which have cut through all of the stratigraphy are sampled at the regional scale, and smaller, shallower scale-bound fractures are not observed on the

digital elevation models used to acquire regional to sub-regional datasets. This would result in an *apparent* strata-bound effect, where the lengths appear to be scale-restricted.

An alternative - and preferred - possibility is that the regional scale data in this study are genuinely better described by an exponential or log-normal distribution. This would imply that a characteristic fracture size exists as has been observed in many strata-bound fracture systems (Odling *et al.* 1999). In the context of crystalline geothermal reservoirs, Massiot *et al.* (2015) have reported such distributions in borehole fractures caused by the presence of lithological layering. In the case of the Negros field volcanic rocks, a characteristic size could be imposed by lithological layering at the largest scale, i.e. the total thickness of the volcanoclastic and other successions. At the regional and sub-regional scales in other published examples, and elsewhere on Negros, stratified rocks are common. In contrast, the reservoir rocks sampled in the SNGF are mostly crystalline extrusive and massive intrusive rocks. Thus, a characteristic length scale might be imposed by the dimensions of the intrusions that act as a limit to the larger fracture lengths. We would caution, however, that the macroscale and mesoscale transects are better constrained than the larger scale datasets because a wider range of fracture sizes were analyzed (i.e. from hand lens 10^{-5} m to whole outcrop 10^1 m). Thus, we are more confident in the scaling relationships observed at these scales.

The disparity in the distribution of the fracture networks in the lineament maps is also evident in the multiscale plot of the cumulative frequency against the length (Figure 4). A break in the scaling exponent slope from -0.90 to -1.70 is noted at the divide between the mesoscale/macroscale and the regional/sub-regional lineament transects. From this plot, it appears that complete continuity is not achieved across the eight length scales. The fracture networks could therefore be described as ‘self affine’, i.e. there is a change in scaling exponent with scale, although this may actually be a result of the mixing of signals at the regional scale versus the smaller scale of datasets as discussed earlier. If fracture length is being inhibited by a characteristic length scaling, this might have the effect of causing steeper scaling exponent. We note that the change in slope occurs between the 100 to 500 m lengths where there is a lack of recorded fracture data. A possibility is that the size limitation-effect is itself length dependent, i.e. larger fractures are more inhibited. This would result in a steeper scaling slope and possible log-normal distribution of the regional scale fractures. Collecting fracture data at the length interval of the slope break (e.g. by using LiDAR scans of cliff sections, for example) could better constrain this slope change and assist in investigating if this is indeed a function of differing mechanical boundaries or whether it is just a data resolution issue. If the slope for these fracture lengths was consistent with those of the regional/sub-regional scales or with the mesoscale/macroscale, it would increase the confidence in constraining the characteristic length that could potentially then be correlated with the stratigraphic thicknesses of the volcanic succession. Ideally, the lineaments also need to be confirmed on the ground as to whether they correspond to natural fractures or not. Then further data and analysis are required to determine the presence of any

characteristic scaling due to host rock mechanical properties and there is a need to constrain the fracture population at regional scales in the reservoir itself.

Other than the scaling implications of the size distribution, the utility of the cumulative fracture intensity versus fracture size plots is straightforward. Aperture for instance has a direct implication for the permeability of a fracture system (Renshaw and Park 1997). Although the conditions are somewhat simplified, volumetric fluid flow in a closed fracture bounded by two smooth parallel walls is suggested to be directly proportional to the cube of the aperture (Klimczak *et al.* 2010; Witherspoon *et al.* 1980). This is the core concept of the cubic law for fluid flow introduced by Witherspoon *et al.* (1980) and was later expanded as a quintic law in Klimczak *et al.* (2010) to consider the square root relationship of length with aperture detailed in Olson (2003). The application of these flow laws must take into account partially filled or non-smooth fractures that are typically seen in geothermal systems (e.g. Sausse 2002).

Odling *et al.* (1999) have shown that fracture orientation, size distribution, intensity, and spatial distribution dictate the connectivity within a fracture network, whilst Sanderson and Nixon (2015) and Manzocchi (2002) have highlighted the important role of fracture intersections, abutments, and splays. In our investigation, the fracture attribute analyses were complemented with topological studies carried out across five dataset scales. Consistently, outcrop datasets gave similar results to well core data. Data from the lineament maps plot on the opposite side of the ternary diagram (Figure 7a), but this is considered to be a sampling issue. The number and type of intersection points or nodes appear to be most controlled by the fracture intensity, particularly of those fractures which do not run parallel to each other, and not by the scale of the observation.

Overall, our findings suggest that the fracture system within the SNGF is dominated by Y-nodes (Figure 7a) which indicates that fractures tend to form abutments and splays, rather than intersecting each other. There is good evidence that the presence of different episodes of fracture formation within the SNGF is related to increased Y- (and some X) node formation. Hence, cross-cutting or abutting relationships are apparently enhanced when fractures of different ages are present, which is consistent with the documented fracturing history of the SNGF (e.g. Pastoriza *et al.* 2018).

Evaluation of the variation of the topology in each dataset scale reveals the presence of geological factors that may have influenced or have been influenced by the topological characteristics. Mineral alteration and topology are particularly correlated in the outcrop scanlines. Evidence of hydrothermal fluids altering the immediate walls of the fractures (in outcrops) or precipitating (veins, particularly in well cores) is higher for fracture populations with more connected node types (e.g. X- and Y-nodes). This further exemplifies the role of fracture connectivity in creating permeability, and illustrates why connected branches are so important in fluid flow. This corroborates the observation that Group 2 fractures are Y-node dominated compared to the Group 1 fractures, and hence, are more connected.

As discussed in Pastoriza *et al.* (2018), presently, Group 2 fractures have mostly remained open or partially open. Hence, they are likely to be better drilling targets than the Group 1 fractures.

Also, at the outcrop scale, it can be seen that connected branches are more abundant close to larger-scale faults. This may reflect a progressive increase in fracture intensity from the background level towards the damage zone, as one moves closer to the fault core. It is suggested that with an increase in fracture intensity, there is a higher probability for non-parallel fractures to intersect which results in a higher abundance of Y-nodes and X-nodes over isolated nodes.

Additionally, fracture systems sampled in boreholes do not show a relationship between depth or lithology and node types. The location of permeable zones also appears to be not directly related to topology, although if these were complemented with other fault indicators (e.g. drilling parameters, mineralogy and rock textures), the results might be better constrained. Lithology and topology in the subsurface also appear to be not related to each other, consistent with the results of Barton and Zoback (1992) where fracture frequency and lithology were also shown to be not correlated.

It has been shown here that the branch type distribution is much more important than the node type distribution. Despite the low numbers of X-nodes in most of the fracture populations studied, more than two thirds of the systems have high C_B values meaning that doubly connected branches are highly probable. Such a system is ideal for good permeability to exist, provided that the fractures have remained completely to partially open.

The disparity between the lineament network with the macroscale and mesoscale fracture network samples also appears in the topology characteristics where lineament connectivity is dominated by intersections, rather than abutments and splays. This reaffirms the resolution issue noted in the size distribution characteristics, where cross-cutting relationships may no longer be observable at the resolution of the digital elevation models used. Potentially, what are in reality Y-nodes may be captured as X-nodes instead.

CONCLUSIONS

Characterizing geothermal reservoir fracture systems almost inevitably involves using the sparse information available to address uncertainty in the nature of the subsurface. In the SNGF where there is a limited availability of subsurface images, consolidation of other datasets and maximization of extracted information from them are required. As result of this work, it was shown that:

- (1) Fracture length and aperture for datasets compiled across six to eight orders of magnitude within the SNGF are best described collectively by a power law relationship, although the regional/sub-regional datasets individually show either a log-normal or exponential distributions;

- (2) The surface fractures are good analogues of the subsurface fracture system based on the similarity of the statistics collected at outcrop and in well cores;
- (3) There is an observed change in the scaling exponent in the 100 to 500 m length-scales which may be an effect of the fractures being restricted along the certain lithological layers or may alternatively be sampling issue;
- (4) The topology data from the SNGF suggest that Y-nodes and doubly-connected branches are dominant, which reveals a fracture system with a high level of connectivity and a potential for significant and highly effective fluid flow.

The amount of information gathered in this work represents a good starting point from which to create fracture network models of the reservoir that could provide a better visualization on how fractures interact and are spatially located to support fluid flow within the SNGF. Further investigation of the regional-scale fracture systems would help to address the question over the upper bounds on the power law scaling in both length and aperture. The approach developed here can be applied to many other fracture-hosted geothermal systems worldwide.

ACKNOWLEDGEMENT

We acknowledge the support of the Energy Development Corporation who also gave access to internal reports and well data. Jonathan Kit Reyes and Ferdinand Castillejo are thanked for their assistance during fieldwork in Negros. Nick Vily Primaleon, Joeffrey Caranto and Francis Sta.Ana gave many constructive criticisms whilst writing the paper, whilst comments by editor Jon Gutmanis and reviewers Owen Callahan and Roberto Rizzo very much helped to improve the manuscript.

FUNDING

This work is part of the PhD thesis of the main author at Durham University, generously funded by the Energy Development Corporation.

REFERENCE CITED

- Antonellini, M., Aydin, A. & Orr, L. 1999. Outcrop-Aided Characterization of a Faulted Hydrocarbon Reservoir: Arroyo Grande Oil Field, California, USA. *Faults and Subsurface Fluid Flow in the Shallow Crust*, 7-26, <http://doi.org/doi:10.1029/GM113p0007>
- Ariceto-Villarosa, H.G., Bueza, E.L., Reyes, A.G. & Zaide-Delfin, M.C. 1988. *The subsurface geology and alteration mineralogy of Nasuji-Sogongon Sector, Southern Negros Geothermal Field*. PNOC-Energy Development Corporation Internal Report.
- Aurelio, M.A. 2000. Shear partitioning in the Philippines: constraints from Philippine fault and global positioning system data. *The Island Arc*, **9**, 584-597.
- Aurelio, M.A., Dianala, J.D.B., Taguibao, K.J.L., Pastoriza, L.R., Reyes, K., Sarande, R. & Lucero Jr, A. 2017. Seismotectonics of the 6 February 2012 Mw 6.7 Negros Earthquake, central

597 Philippines. *Journal of Asian Earth Sciences*, **142**, 93-108,
598 <http://doi.org/http://dx.doi.org/10.1016/j.jseaes.2016.12.018>.

599

600 Bär, K., Felder, M., Götz, A.E., Molenaar, N. & Sass, I. 2011. The Rotliegend Reservoir System of
601 the Northern Upper Rhine Graben, Germany: From Outcrop Analogue Studies to Geothermal
602 Reservoir Assessment. *AAPG Search and Discovery Article*, **80194**.

603 Barton, C.A. & Zoback, M.D. 1992. Self-similar distribution and properties of macroscopic fractures
604 at depth in crystalline rock in the Cajon Pass Scientific Drill Hole. *Journal of Geophysical*
605 *Research: Solid Earth*, **97**, 5181-5200, <http://doi.org/10.1029/91jb01674>.

606 Bauer, J.F., Krumbholz, M., Meier, S. & Tanner, D.C. 2017. Predictability of properties of a fractured
607 geothermal reservoir: the opportunities and limitations of an outcrop analogue study. *Geothermal*
608 *Energy*, **5**, 24, <http://doi.org/10.1186/s40517-017-0081-0>.

609 Bayon, F.E.B. & Ogena, M.S. 2005. Handling the problem of rapid reinjection returns in Palinpinon-I
610 and Tongonan, Philippines. *World Geothermal Congress*, Antalya, Turkey.

611 Bonnet, E., Bour, O., Odling, N.E., Davy, P., Main, I., Cowie, P. & Berkowitz, B. 2001. Scaling of
612 fracture systems in geological media. *Reviews of Geophysics*, **39**, 347-383,
613 <http://doi.org/10.1029/1999rg000074>.

614 Chesnaux, R., Allen, D.M. & Jenni, S. 2009. Regional fracture network permeability using outcrop
615 scale measurements. *Engineering Geology*, **108**, 259-271,
616 <http://doi.org/https://doi.org/10.1016/j.enggeo.2009.06.024>.

617 Clark, R.M., Cox, S.J.D. & Laslett, G.M. 1999. Generalizations of power-law distributions applicable
618 to sampled fault-trace lengths: model choice, parameter estimation and caveats. *Geophysical*
619 *Journal International*, **136**, 357-372, <http://doi.org/10.1046/j.1365-246X.1999.00728.x>.

620 Clauset, A., Shalizi, C.R. & Newman, M.E.J. 2009. Power-law distributions in empirical data. *SIAM*
621 *Review*, **51**, 661-703, <http://doi.org/10.1137/070710111>.

622 Gillespie, P.A., Howard, C.B., Walsh, J.J. & Watterson, J. 1993. Measurement and characterisation of
623 spatial distributions of fractures. *Tectonophysics*, **226**, 113-141,
624 [http://doi.org/http://dx.doi.org/10.1016/0040-1951\(93\)90114-Y](http://doi.org/http://dx.doi.org/10.1016/0040-1951(93)90114-Y).

625 Gillespie, P.A., Johnston, J.D., Loriga, M.A., McCaffrey, K.J.W., Walsh, J.J. & Watterson, J. 1999.
626 Influence of layering on vein systematics in line samples. *Geological Society, London, Special*
627 *Publications*, **155**, 35-56, <http://doi.org/10.1144/gsl.sp.1999.155.01.05>.

628 Gross, M.R., Gutierrez-Alonso, G., Bai, T., Wacker, M.A., Collinsworth, K.B. & Behl, R.J. 1997.
629 Influence of mechanical stratigraphy and kinematics on fault scaling relations. *Journal of*
630 *Structural Geology*, **19**, 171-183, [http://doi.org/http://dx.doi.org/10.1016/S0191-8141\(96\)00085-](http://doi.org/http://dx.doi.org/10.1016/S0191-8141(96)00085-5)
631 [5](http://doi.org/http://dx.doi.org/10.1016/S0191-8141(96)00085-5).

632 Guerriero, V., Iannace, A., Mazzoli, S., Parente, M., Vitale, S. & Giorgioni, M. 2010. Quantifying
633 uncertainties in multi-scale studies of fractured reservoir analogues: Implemented statistical
634 analysis of scan line data from carbonate rocks. *Journal of Structural Geology*, **32**, 1271-1278,
635 <http://doi.org/http://dx.doi.org/10.1016/j.jsg.2009.04.016>.

636 Hooker, J.N., Laubach, S.E. & Marrett, R. 2014. A universal power-law scaling exponent for fracture
637 apertures in sandstones. *Geological Society of America Bulletin*,
638 <http://doi.org/10.1130/b30945.1>.

639 Jarvis, A., Reuter, H.I., Nelson, A. & Guevara, E. 2008. Hole-filled SRTM for globe Version 4,
640 available from the CGIAR-CSI SRTM 90m Database.

641 Klimczak, C., Schultz, R.A., Parashar, R. & Reeves, D.M. 2010. Cubic law with aperture-length
642 correlation: implications for network scale fluid flow. *Hydrogeology Journal*, **18**, 851-862,
643 <http://doi.org/10.1007/s10040-009-0572-6>.

644
645 Ledésert, B., Dubois, J., Genter, A. & Meunier, A. 1993. Fractal analysis of fractures applied to
646 Soultz-sous-Forêts hot dry rock geothermal program. *Journal of Volcanology and Geothermal*
647 *Research*, **57**, 1-17, [http://doi.org/http://dx.doi.org/10.1016/0377-0273\(93\)90028-P](http://doi.org/http://dx.doi.org/10.1016/0377-0273(93)90028-P).

648 Lin, J.-Y. & Lo, C.-L. 2013. Earthquake-induced crustal gravitational potential energy change in the
649 Philippine area. *Journal of Asian Earth Sciences*, **66**, 215-223,
650 <http://doi.org/http://dx.doi.org/10.1016/j.jseaes.2013.01.009>.

651 Mäkel, G.H. 2007. The modelling of fractured reservoirs: constraints and potential for fracture
652 network geometry and hydraulics analysis. *Geological Society, London, Special Publications*,
653 **292**, 375-403, <http://doi.org/10.1144/sp292.21>.

654 Manzocchi, T. 2002. The connectivity of two-dimensional networks of spatially correlated fractures.
655 *Water Resources Research*, **38**, 1-1-1-20, <http://doi.org/10.1029/2000wr000180>.

656 Marrett, R., Ortega, O.J. & Kelsey, C.M. 1999. Extent of power-law scaling for natural fractures in
657 rock. *Geology*, **27**, 799-802, [http://doi.org/10.1130/0091-7613\(1999\)027<0799:eoplsf>2.3.co;2](http://doi.org/10.1130/0091-7613(1999)027<0799:eoplsf>2.3.co;2).

658 Massiot, C., McNamara, D.D., Nicol, A. & Townend, J. 2015. Fracture width and spacing
659 distributions from borehole televiewer logs and cores in the Rotokawa Geothermal Field, New
660 Zealand. *Proceedings World Geothermal Congress*, Melbourne, Australia.

661 McCaffrey, K.J.W. & Johnston, J.D. 1996. Fractal analysis of a mineralised vein deposit: Curraghinalt
662 gold deposit, County Tyrone. *Mineralium Deposita*, **31**, 52-58,
663 <http://doi.org/10.1007/bf00225395>.

664 Odling, N.E., Gillespie, P., Bourguine, B., Castaing, C., Chiles, J.P., Christensen, N.P., Fillion, E.,
665 Genter, A., *et al.* 1999. Variations in fracture system geometry and their implications for fluid
666 flow in fractures hydrocarbon reservoirs. *Petroleum Geoscience*, **5**, 373-384,
667 <http://doi.org/10.1144/petgeo.5.4.373>.

668 Olson, J.E. 2003. Sublinear scaling of fracture aperture versus length: An exception or the rule?
669 *Journal of Geophysical Research: Solid Earth*, **108**, <http://doi.org/10.1029/2001jb000419>.

670 Ortega, O.J., Marrett, R.A. & Laubach, S.E. 2006. A scale-independent approach to fracture intensity
671 and average spacing measurement. *AAPG Bulletin*, **90**, 193-208.

672 Pastoriza, L.R. 2017. *The geological characterisation and permeability evaluation of fractures in the*
673 *Southern Negros Geothermal Field, Negros Island, Philippines*. Doctoral Thesis, University of
674 Durham.

675 Pastoriza, L.R., Holdsworth, R.E., McCaffrey, K.J.W. & Dempsey, E. 2018. Tectonic Evolution of
676 the Southern Negros Geothermal Field and Implications for the Development of Fractured
677 Geothermal Systems. *Geofluids*, **2018**, 20, <http://doi.org/10.1155/2018/6025038>.

678 Pickering, G., Bull, J.M. & Sanderson, D.J. 1995. Sampling power-law distributions. *Tectonophysics*,
679 **248**, 1-20, [http://doi.org/https://doi.org/10.1016/0040-1951\(95\)00030-Q](http://doi.org/https://doi.org/10.1016/0040-1951(95)00030-Q).

680 Pless, J.C. 2012. *Characterising fractured basement using the Lewisian Gneiss Complex, NW*
681 *Scotland: Implications for fracture systems in the Clair Field basement*. PhD Geology E-Theses,
682 Durham University.

683 Rae, A.J., Cooke, D.R., Phillips, D. & Zaide-Delfin, M. 2004. The nature of magmatism at Palinpinon
684 geothermal field, Negros Island, Philippines: implications for geothermal activity and regional

685 tectonics. *Journal of Volcanology and Geothermal Research*, **129**, 321-342,
686 [http://doi.org/http://dx.doi.org/10.1016/S0377-0273\(03\)00280-4](http://doi.org/http://dx.doi.org/10.1016/S0377-0273(03)00280-4).

687 Rangin, C. 2016. Rigid and non-rigid micro-plates: Philippines and Myanmar-Andaman case studies.
688 *Comptes Rendus Geoscience*, **348**, 33-41,
689 <http://doi.org/http://dx.doi.org/10.1016/j.crte.2015.10.008>.

690
691 Rangin, C., Le Pichon, X., Mazzotti, S., Pubellier, M., Chamot-Rooke, N., Aurelio, M., Walpersdorf,
692 A. & Quebral, R. 1999. Plate convergence measured by GPS across the Sundaland/Philippine
693 Sea Plate deformed boundary: the Philippines and eastern Indonesia. *Geophysical Journal*
694 *International*, **139**, 296-316, <http://doi.org/10.1046/j.1365-246x.1999.00969.x>.

695 Renshaw, C.E. & Park, J.C. 1997. Effect of mechanical interactions on the scaling of fracture length
696 and aperture. *Nature*, **386**, 482-484.

697 Rizzo, R.E., Healy, D. & De Siena, L. 2017. Benefits of maximum likelihood estimators for fracture
698 attribute analysis: Implications for permeability and up-scaling. *Journal of Structural Geology*,
699 **95**, 17-31, <http://doi.org/http://dx.doi.org/10.1016/j.jsg.2016.12.005>.

700 Rohrbaugh, M.B., Dunne, W.M. & Mauldon, M. 2002. Estimating fracture trace intensity, density,
701 and mean length using circular scan lines and windows. *AAPG Bulletin*, **86**, 16.

702 Sanderson, D.J. & Nixon, C.W. 2015. The use of topology in fracture network characterization.
703 *Journal of Structural Geology*, **72**, 55-66,
704 <http://doi.org/http://dx.doi.org/10.1016/j.jsg.2015.01.005>.

705 Sausse, J. 2002. Hydromechanical properties and alteration of natural fracture surfaces in the Soultz
706 granite (Bas-Rhin, France). *Tectonophysics*, **348**, 169-185,
707 [http://doi.org/https://doi.org/10.1016/S0040-1951\(01\)00255-4](http://doi.org/https://doi.org/10.1016/S0040-1951(01)00255-4).

708 Scholz, C.H. 1987. Wear and gouge formation in brittle faulting. *Geology*, **15**, 493-495,
709 [http://doi.org/10.1130/0091-7613\(1987\)15<493:wagfib>2.0.co;2](http://doi.org/10.1130/0091-7613(1987)15<493:wagfib>2.0.co;2).

710 USGS 2012. Magnitude 6.7-Negros-Cebu Region, Philippines.
711 <http://earthquake.usgs.gov/earthquakes/eqinthenews/2012/usb0007wgq/>.

712 Walsh, J., Watterson, J. & Yielding, G. 1991. The importance of small-scale faulting in regional
713 extension. *Nature*, **351**, 391-393.

714 Watanabe, K. & Takahashi, H. 1995. Fractal geometry characterization of geothermal reservoir
715 fracture networks. *Journal of Geophysical Research: Solid Earth*, **100**, 521-528,
716 <http://doi.org/10.1029/94jb02167>.

717 Watkins, H., Bond, C.E., Healy, D. & Butler, R.W.H. 2015. Appraisal of fracture sampling methods
718 and a new workflow to characterise heterogeneous fracture networks at outcrop. *Journal of*
719 *Structural Geology*, **72**, 67-82, <http://doi.org/http://dx.doi.org/10.1016/j.jsg.2015.02.001>.

720 Wennberg, O.P., Azizzadeh, M., Aqrawi, A.A.M., Blanc, E., Brockbank, P., Lyslo, K.B., Pickard, N.,
721 Salem, L.D., *et al.* 2007. The Khaviz Anticline: an outcrop analogue to giant fractured Asmari
722 Formation reservoirs in SW Iran. *Geological Society, London, Special Publications*, **270**, 23-42.

723 Weydt, L.M., Bär, K., Colombero, C., Comina, C., Deb, P., Lepillier, B., Mandrone, G., Milsch, H., *et*
724 *al.* 2018. Outcrop analogue study to determine reservoir properties of the Los Humeros and
725 Acoculco geothermal fields, Mexico. *Adv. Geosci.*, **45**, 281-287, [http://doi.org/10.5194/adgeo-](http://doi.org/10.5194/adgeo-45-281-2018)
726 [45-281-2018](http://doi.org/10.5194/adgeo-45-281-2018).

727 Witherspoon, P.A., Wang, J.S.Y., Iwai, K. & Gale, J.E. 1980. Validity of Cubic Law for fluid flow in
728 a deformable rock fracture. *Water Resources Research*, **16**, 1016-1024,
729 <http://doi.org/10.1029/WR016i006p01016>.

Zaide, M. 1984. Interpretation of rock-dating results in the Southern Negros Geothermal Field.
PNOC-EDC Internal Report.

Zeeb, C., Gomez-Rivas, E., Bons, P.D. & Blum, P. 2013. Evaluation of sampling methods for fracture
network characterization using outcrops. *AAPG Bulletin*, **97**, 1545-1566,
<http://doi.org/10.1306/02131312042>

FIGURE CAPTIONS

Figure 1. Geology of the Southern Negros Geothermal Field (modified from Pastoriza *et al.* 2018). (a) Negros Island, showing the Negros volcanic arc in red triangles and the estimated trace of Yupisan Fault in dashed dark pink, overlain by the approximate boundaries of the tectono-stratigraphic terranes. Red box represents the boundaries of Figure 1b. Inset shows the major tectonic structures of the Philippines after Aurelio (2000). (b) Simplified map of SNGF encompassing the CDN volcanic complex showing the key lineaments identified in this study (black line), course of Okoy River (blue), volcanic edifices within the complex (red triangle), and estimated location of thermal manifestations (red dots), overlain by a simplified geological map of the field from Rae *et al.* (2004) and PNOC-EDC internal reports. (c) Geological column of the CDN volcano as encountered in the boreholes. Corresponding ages are in the first column, whilst their general lithologies are in the third column. Note that although there is strong geochronological evidence that the Nasuji Pluton is younger, there is no clear evidence of its intrusion into the younger lithologies

Figure 2. Summary of the palaeostress analysis results per stage of deformation (modified from Pastoriza *et al.* 2018). At the top are the stereographic projection of the key faults per stage with their corresponding slickenlines, where observed. Hollow symbols indicate a component of reverse sense of motion. Cyan stars represent poles of the tensile fractures. The illustrated Stage 2 and Stage 3 results are from the data which have been weighted by both the fault thickness and length as discussed in Pastoriza *et al.* 2018. The compression arrows in Stage 2 and Stage 3 are intended to be smaller to highlight that the associated stress regime is generally extensional. The question mark in the regional present-day direction indicates that only the maximum compression direction is given in the cited study. The smaller arrows are assumed.

Figure 3. Typical set-up of a linear scanline and fracture topology sampling. (a) For regional sub-regional lineaments, transects were done in ArcMap and GME. (b) Rose diagram of the picked lineaments. (c) Linear transects in outcrops (macroscale) and (d) well cores (mesoscale). In (d) well cores, the orientation of fractures is described using theta. (e) Parts of a fracture array typically includes series of lines which when intersect each other form nodes (points of intersection, in circles), and branches, which describe the topology.

Figure 4. Fracture intensity (right y-axis) versus length (x-axis) plot. Average spacing is also shown on the left-hand y-axis, which is simply the inverse of fracture intensity. Fractures are coloured according to the scale of observation. Solid trendline and equation are generated from the MLE method.

Figure 5. Fracture intensity (right y-axis) versus aperture (x-axis) plots. Average spacing is also shown on the left hand y-axis, which is simply the inverse of the fracture intensity. Fractures are coloured according to the scale of observation. Solid trendline and equation are generated from the MLE method.

Figure 6. Number of nodes (y-axis) plotted against the scanline diameter in meters (x-axis) observed across all the 70 circular samples. Points are coloured according to the scale – regional/sub-regional(yellow), photograph-based macroscale (blue), field-based macroscale (grey), mesoscale (red), slab hand samples(green), and microscale (pink).

Figure 7. (a) Node type ternary diagram of all the fracture intersection data populations, coloured according to the scale – regional/sub-regional(yellow), photograph-based macroscale (blue), field-based macroscale (grey), mesoscale (red), slab hand samples(green), and microscale (pink). (b) Histogram of the N_B/N_L values with relative frequency as the y-axis.

Figure 8. Node type ternary plots for the circular scanlines carried out in the field exposures/mesoscale. (a) Scanlines performed on both in photographs (red symbols) and in the field (blue symbols). (b) Data sorted according to whether they are related to any alteration (red circles) or not (blue circles). (c) Data grouped based on being situated close to a major fault (red circles) or otherwise (blue circles). (d) Scanlines classified according to which group of fractures they belong to as defined in Pastoriza *et al.* (2018). Group 1 fractures are in blue whilst Group 2 are in red. The circles are samples from the same outcrop (OC-118) whilst the crosses are from other outcrops.

Figure 9. Node type ternary plots of the circular scanlines carried out in the well cores/mesoscale classified in four different ways. (a) According to the rock type - andesite (red circles), intrusive rock (blue circles), clastic rocks (green). (b) According to whether a permeable zone has been detected within the sampling depth – major zone (red), minor zone (purple), no detected zone (black). Note that not all cores are plotted here because some samples were collected at cased off depths, hence, are not part of the spinner survey tests. (c) According to whether the fracture arrays are vein-dominated (red circles) or not (blue). (d) According to the depth where the sample was collected.

Figure 10. (a) Ternary diagram of the probability of the branch types of all the samples, points colored according to the scale of observation - regional/sub-regional(yellow), photograph-based macroscale (blue), field-based macroscale (grey), mesoscale (red), slab hand samples(green), and microscale (pink).

TABLES

Table 1. Summary of field characteristics of the two fracture groups mapped in the area of study (after Pastoriza et al., 2018).

	Group 1	Group 2
Fault rocks	Cohesive and cemented (cataclastic)	Generally non-cohesive/poorly cemented Open fractures in some cases
Key alteration minerals	Abundant pyrite Amorphous silica Quartz rare Cu-sulfides	Abundant clays Quartz Sulphur Zeolites, calcites, gypsum
Orientation/ Kinematics	Mostly E-W sinistral	Mostly NW-SE oblique dextral
Host rocks	Older Southern Negros Fm. Host has been completely altered	All lithologies Both altered and fresh rocks
Other key observations		Usually related to recent (active/inactive) thermal activity seen at the surface

Table 2. General transect information across the three scales of dataset. Transect length for well cores have been corrected by the Terzhagi value.

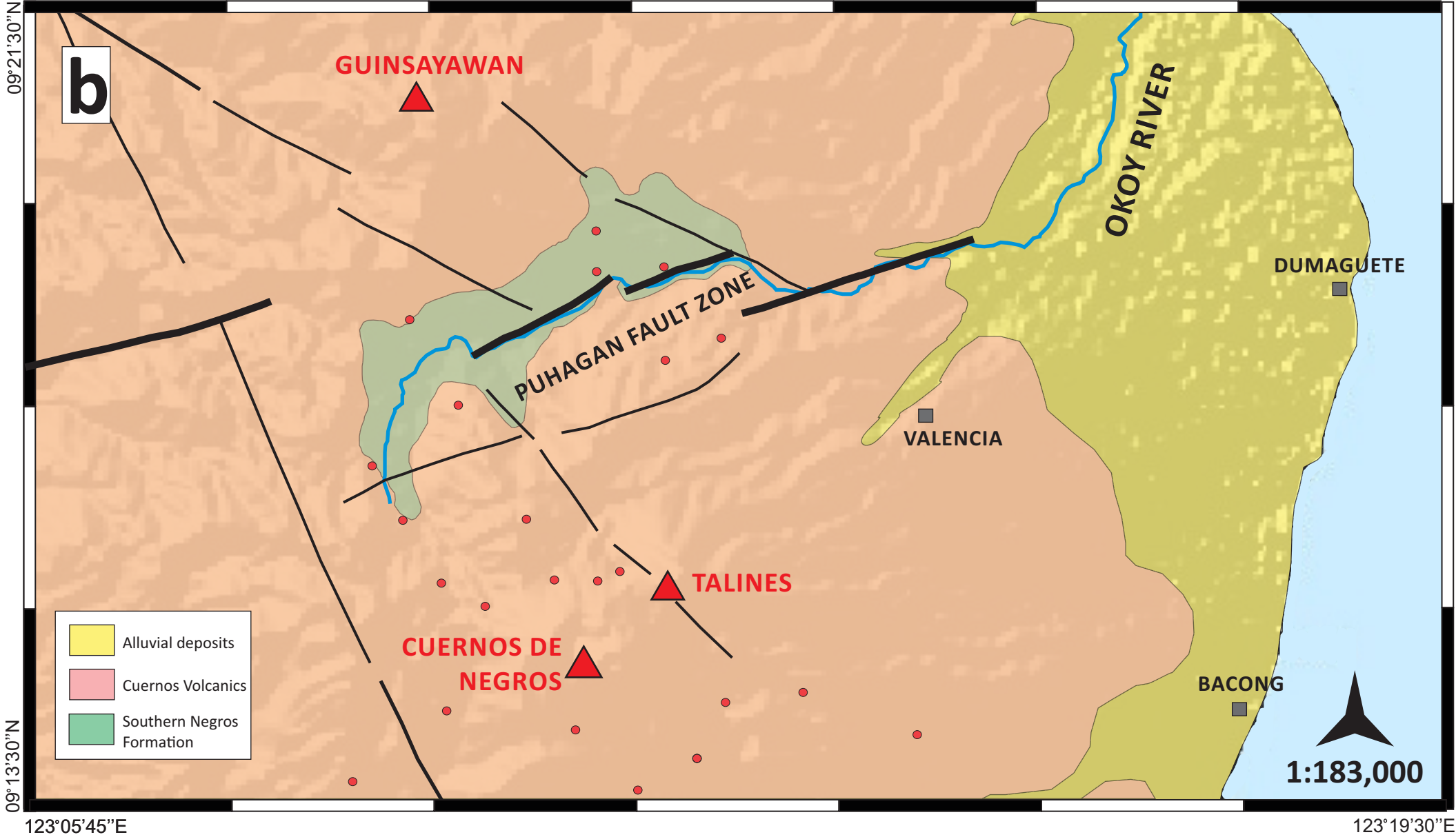
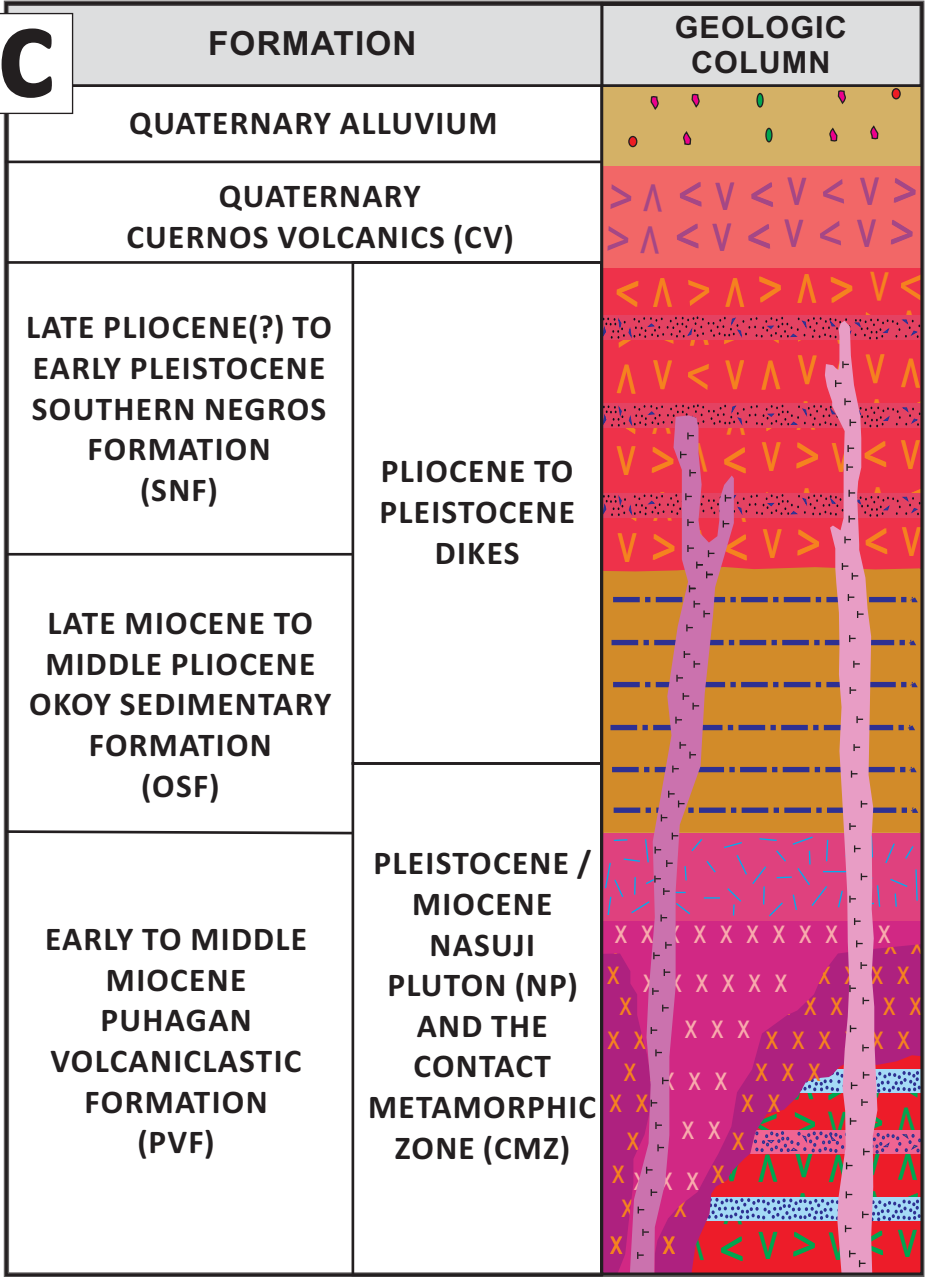
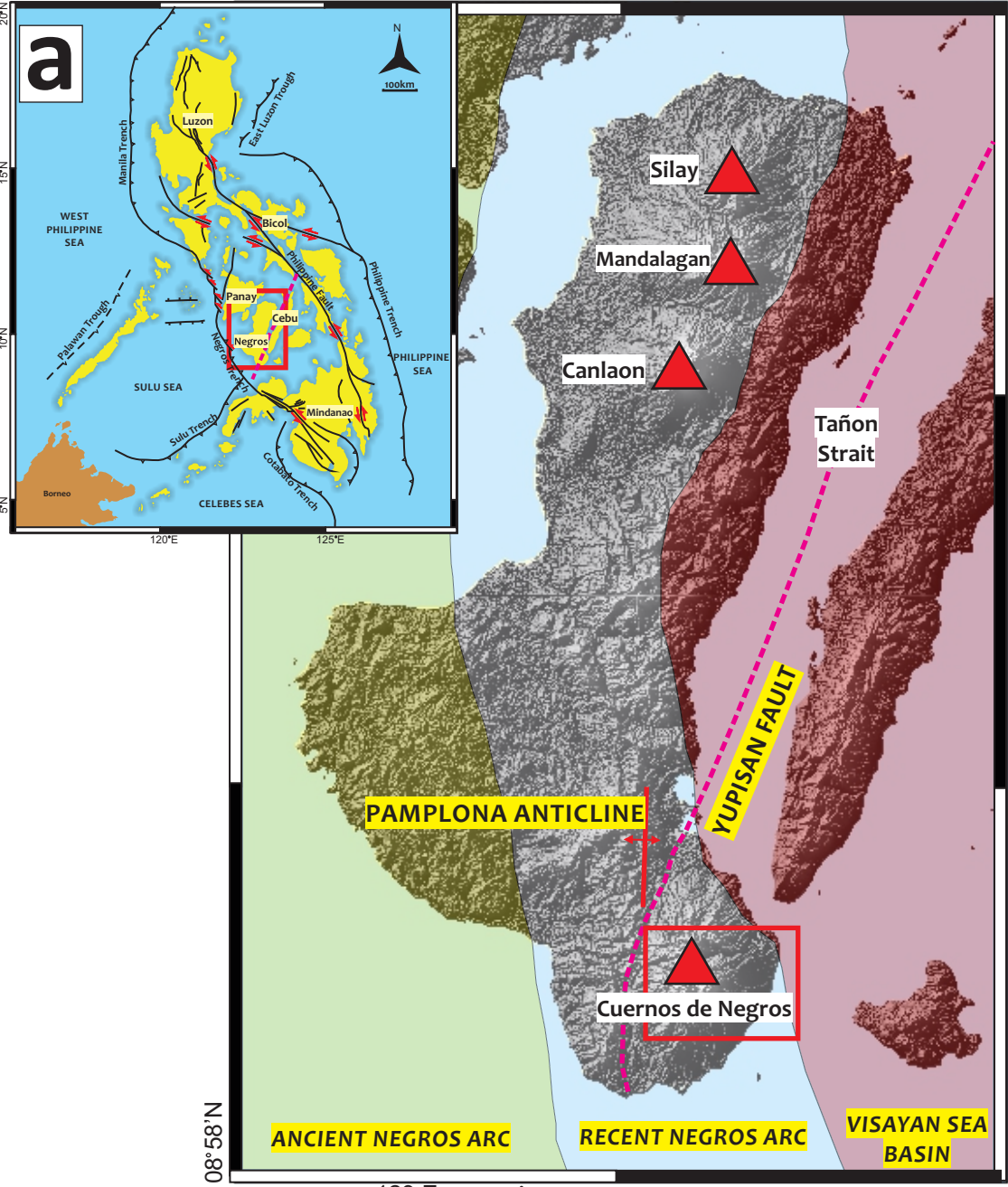
Scale	Transect Code	Lithological Formation*	Number of samples	Length of Transect, m	Mean Fracture intensity, m ⁻¹	Coefficient of variation, C _v	
Regional	500K-NS	N/A	22	118,024.59	1.86E-04	0.79	
	500K-EW		9	36,172.73	2.49E-04	0.53	
	500K-NESW		7	37,767.63	1.85E-04	0.57	
	500K-NWSE		27	105,915.30	2.55E-04	0.65	
	250K-NS	N/A	22	190,450.50	1.16E-04	2.12	
	250K-EW		7	23,086.60	3.03E-04	1.04	
	250K-NESW		6	33,857.93	1.77E-04	0.64	
	250K-NWSE		22	98,751.63	2.23E-04	0.87	
Sub-regional	100K-NS	N/A	29	16,361.25	1.77E-03	1.07	
	100K-EW		17	15,594.83	1.09E-03	1.01	
	100K-NESW		33	20,887.77	1.58E-03	0.83	
	100K-NWSE		27	18,826.16	1.43E-03	1.02	
	50K-NS	N/A	32	15,987.60	2.00E-03	0.84	
	50K-EW		14	15,192.57	9.22E-04	1.06	
	50K-NESW		27	20,594.64	1.31E-03	0.76	
	50K-NWSE		24	20,099.65	1.19E-03	0.91	
	20K-NS	N/A	25	15,814.40	1.58E-03	0.78	
	20K-EW		12	6,648.82	1.80E-03	0.5	
	20K-NESW		26	13,481.33	1.93E-03	1.12	
	20K-NWSE		25	12,752.88	1.96E-03	0.96	
Macroscale	Outside of SNGF	young volcanics	OC-15	102	35.05	2.91E+00	1.47
			OC-17	100	4.77	2.10E+01	1.1
			OC-18	77	15.67	4.92E+00	1.37
	Within SNGF	OC-74	SNF	136	15.08	9.02E+00	2.41
		OC-81	CV	113	24.32	4.65E+00	1.22
		OC-98	SNF	77	8.93	8.62E+00	0.94
		OC-105	CV	37	24.08	1.54E+00	0.8
		OC-107	CV	108	6.43	1.68E+01	1.18
Mesoscale	W1-2	SNF	43	0.29	1.49E+02	1.14	
	W1-3	SNF	10	0.26	3.88E+01	0.43	
	W2-2	NP	17	0.34	5.07E+01	1.03	
	W3-1	CMZ	30	0.17	1.76E+02	1	
	W4-3	NP	17	0.34	5.00E+01	1.09	
	W4-4	NP	11	0.21	5.14E+01	0.99	
	W5-1	NP	33	0.1	3.27E+02	1.26	
	W6-5	NP	12	0.15	8.16E+01	1.4	
	W7-1	SNF	14	0.08	1.85E+02	0.81	

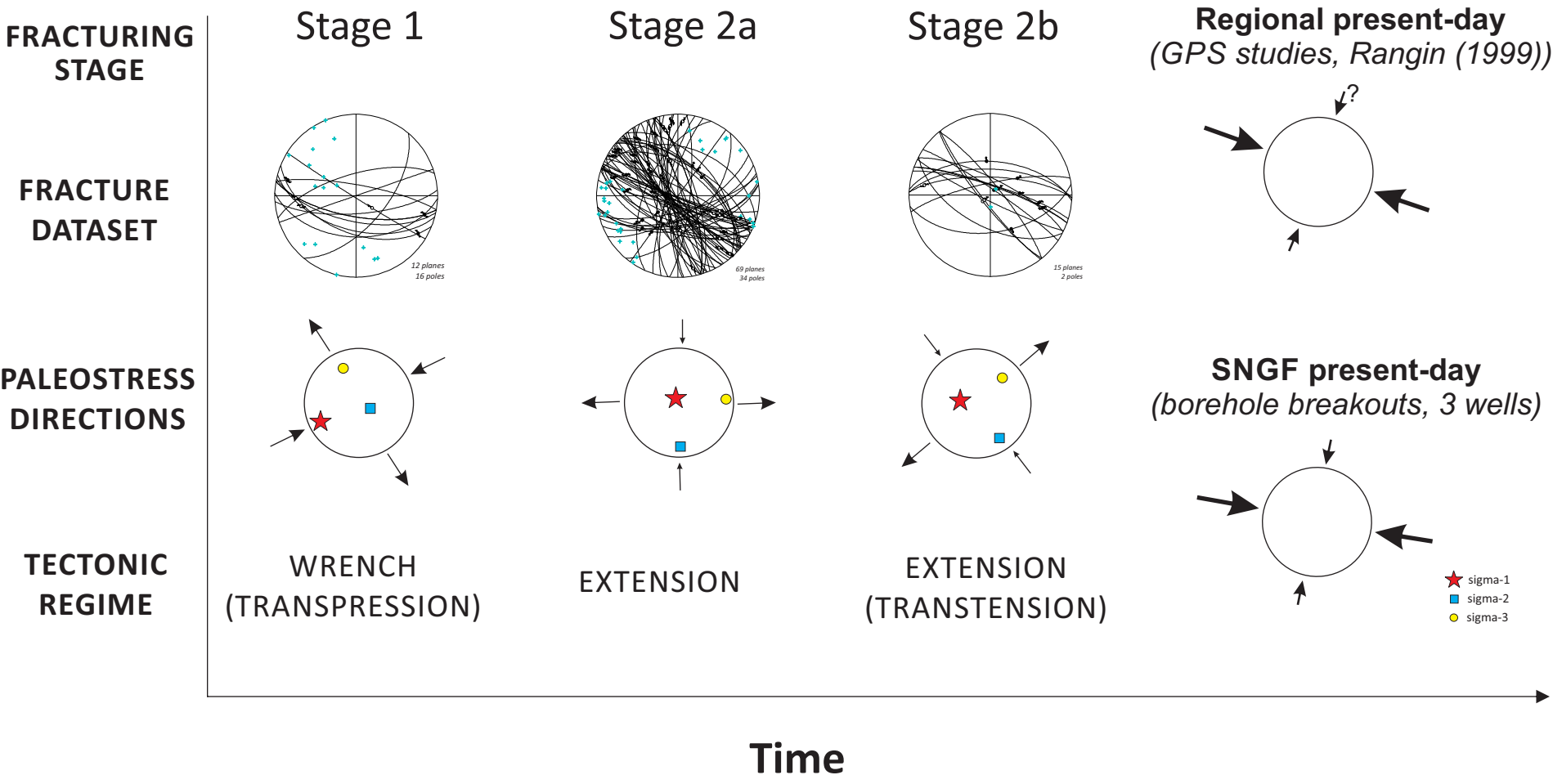
	W7-3	OSF	12	0.21	5.71E+01	1.12
	W8-5	NP	14	0.14	9.81E+01	1.25
	W9-3	NP	33	0.14	2.38E+02	1.53

808 *local lithological formations: SNF – Southern Negros Formation; OSF – Okoy Sedimentary Formation; NP –
809 Nasuji Pluton; CMZ – Contact Metamorphic Zone

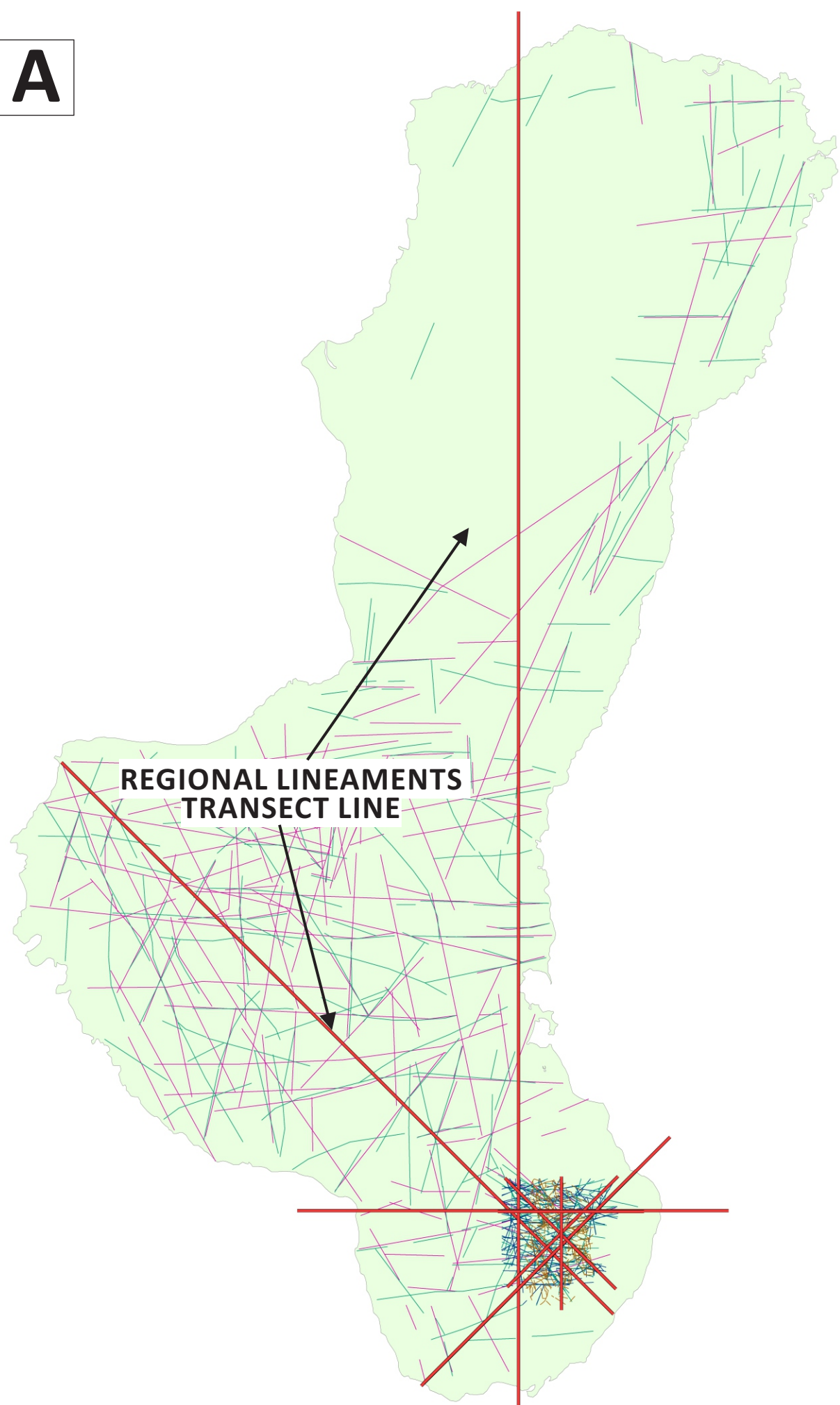
810

811

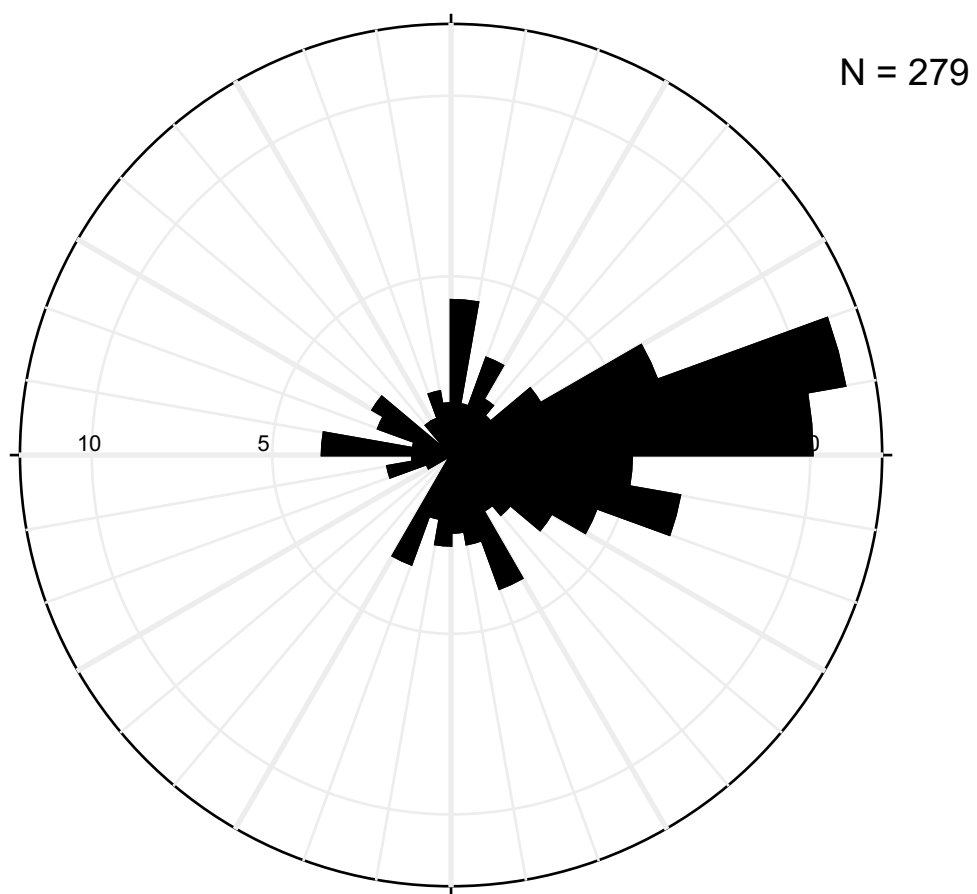




A



B



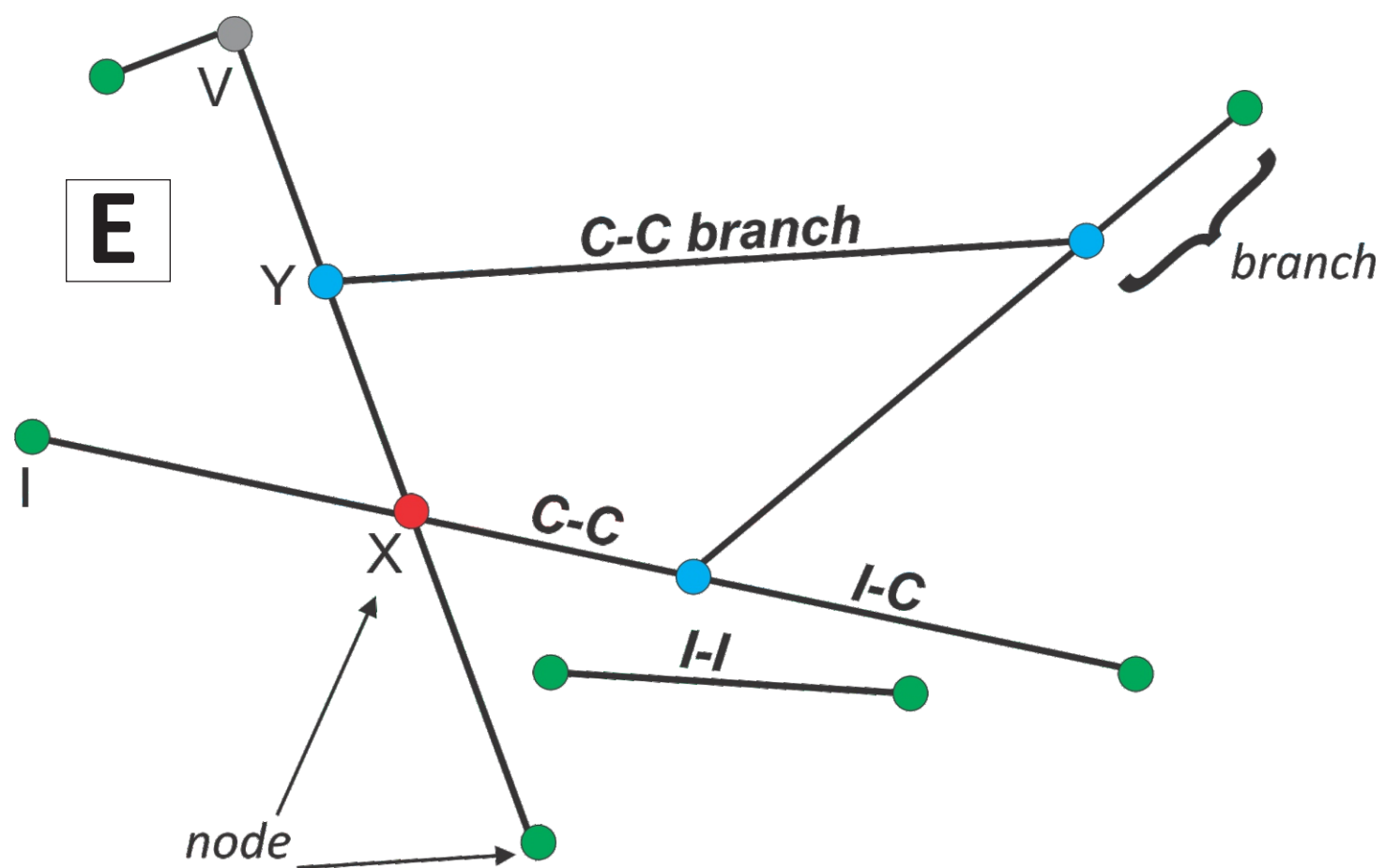
C

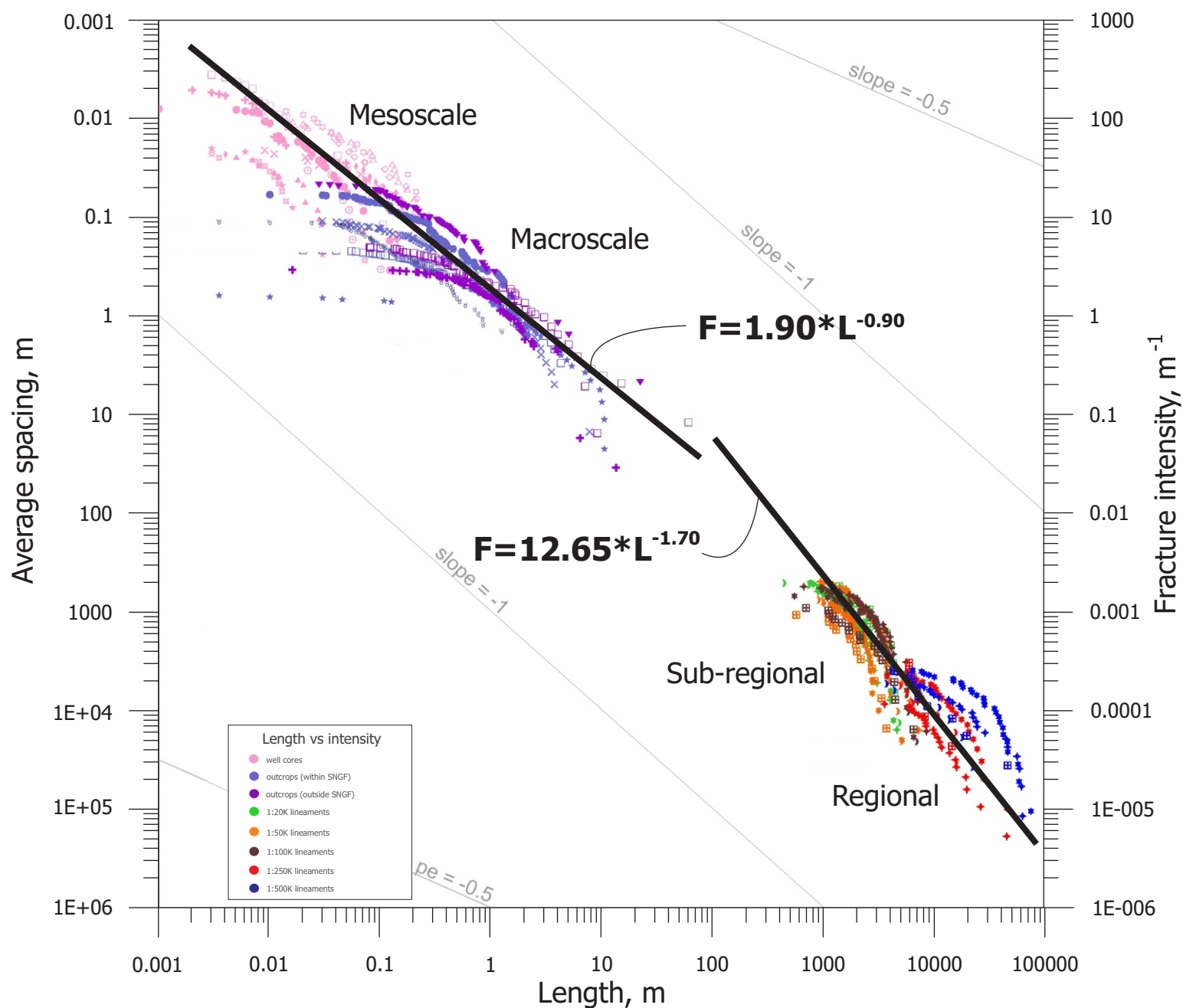


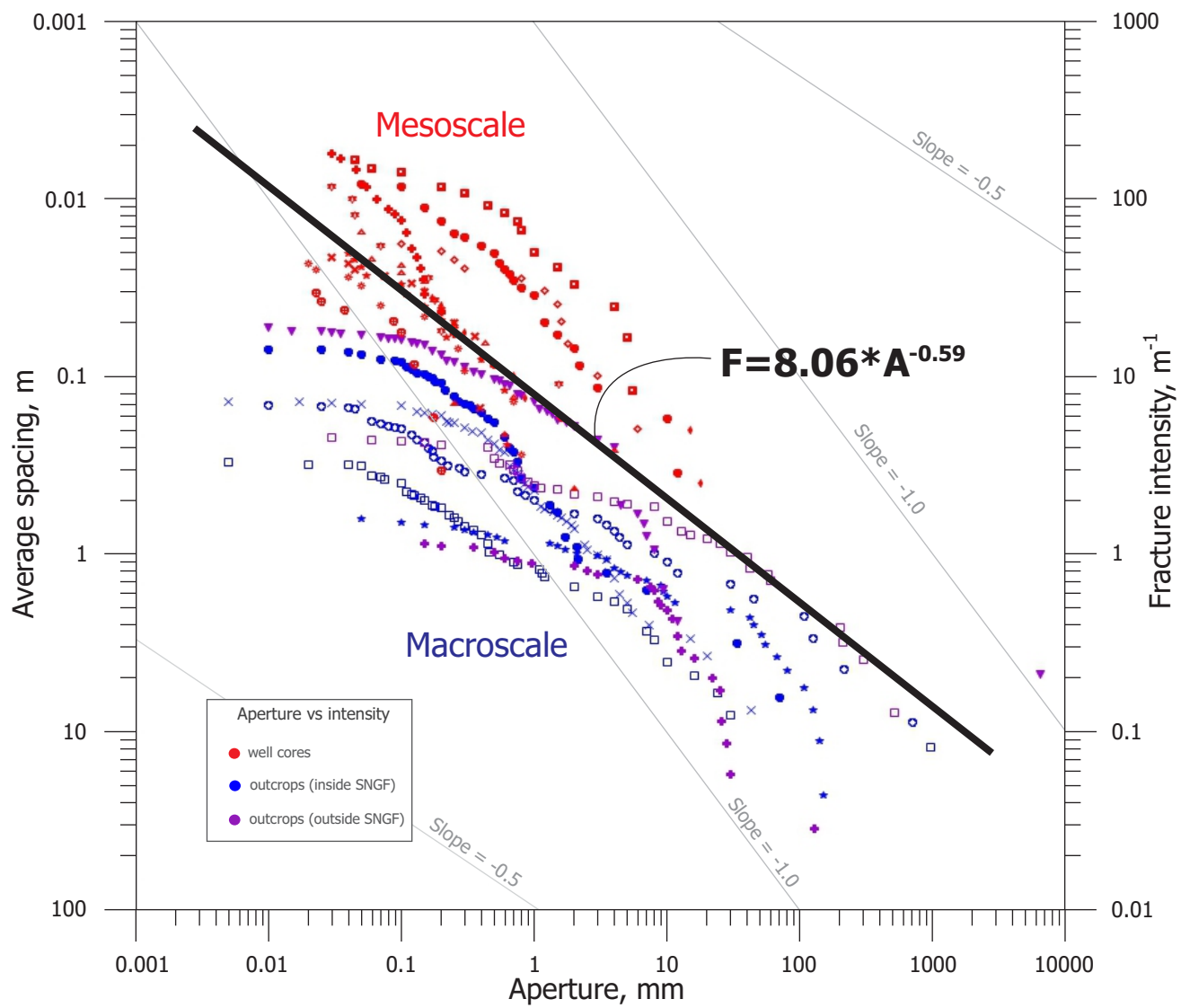
D

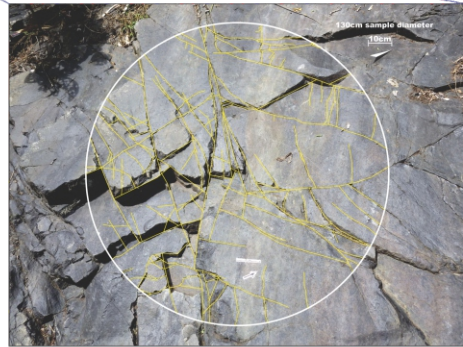
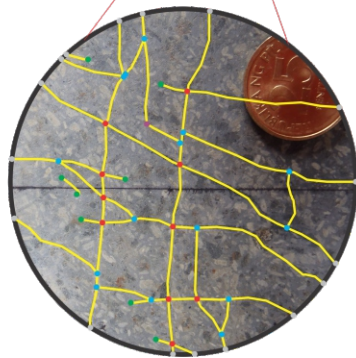
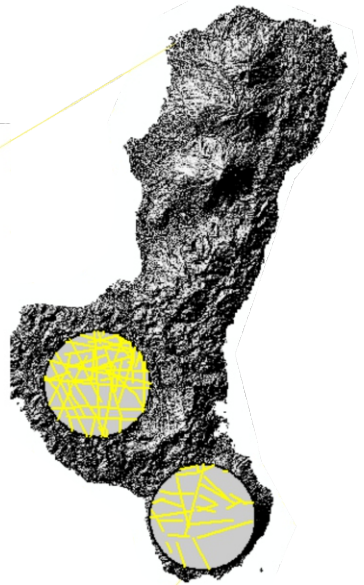
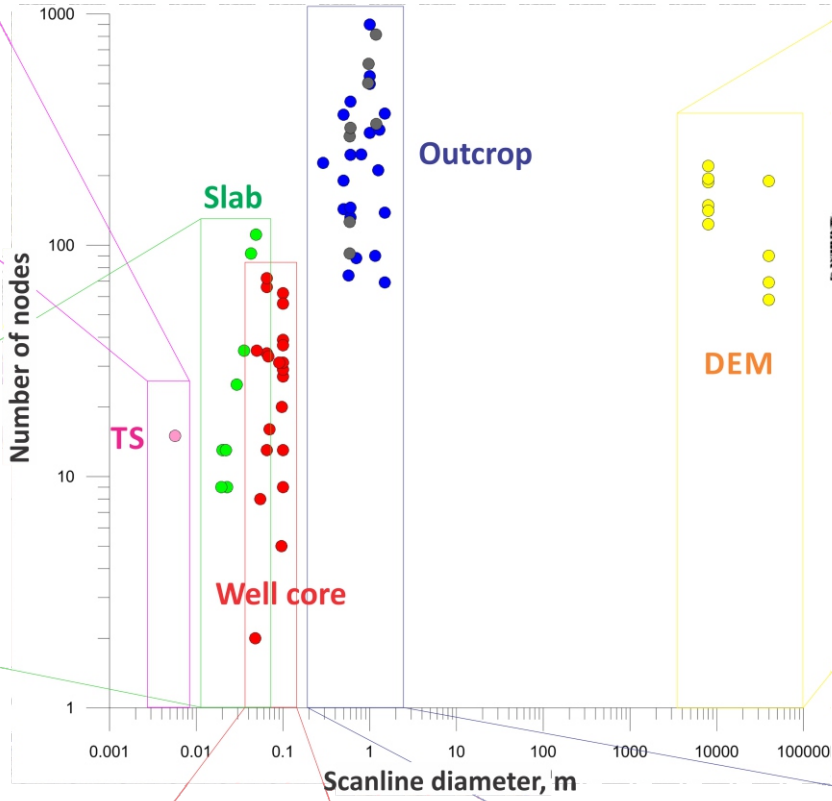
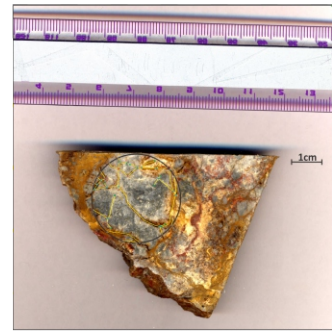
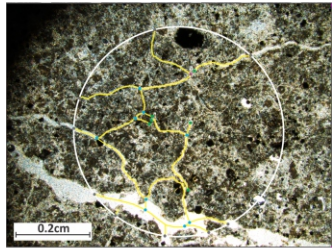


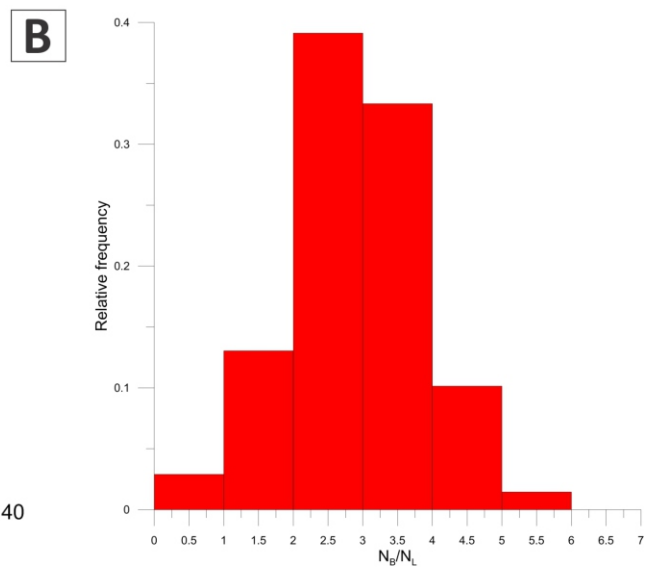
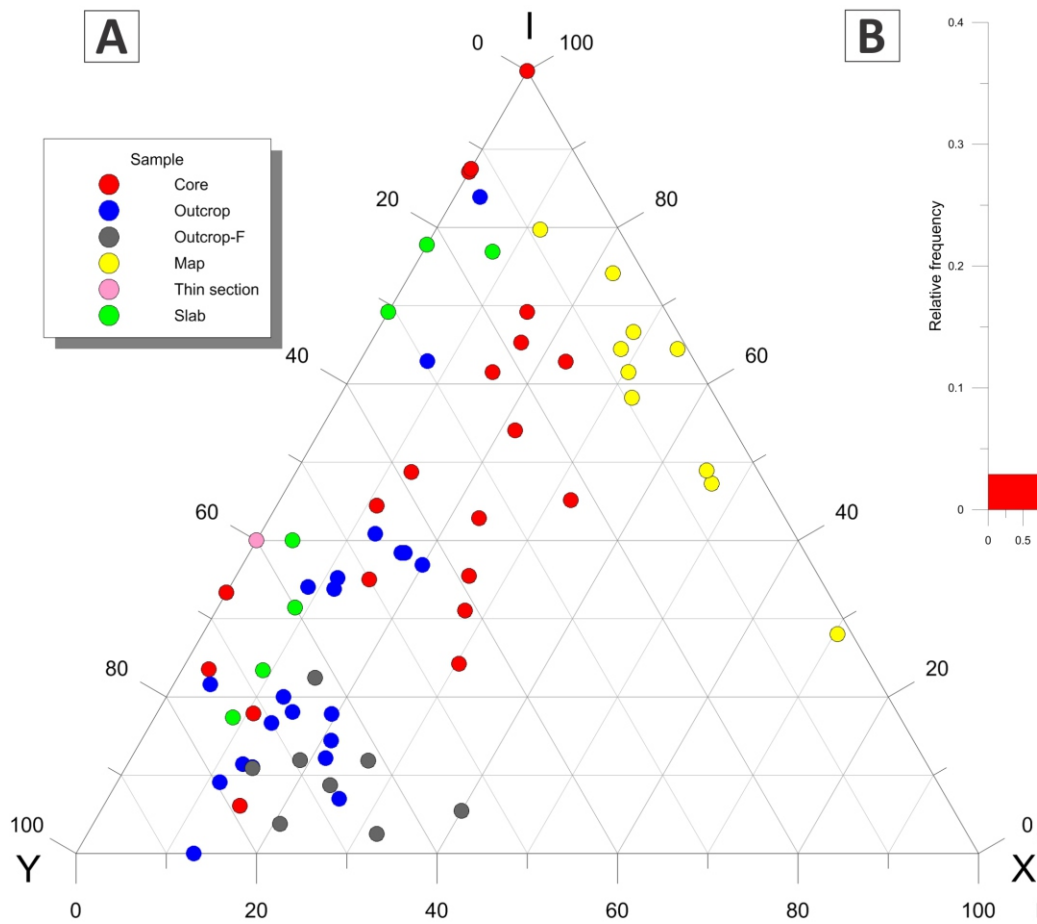
E

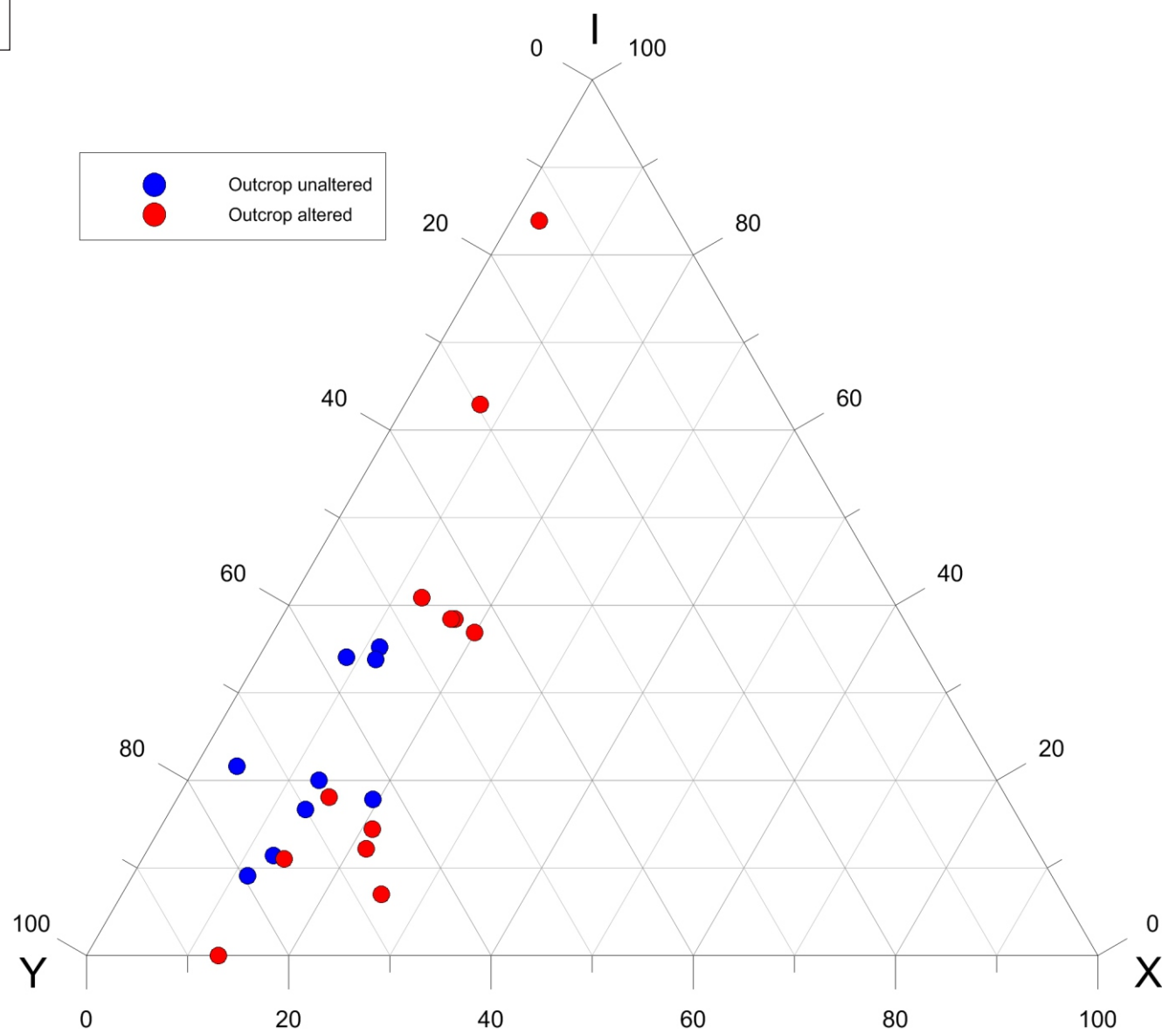
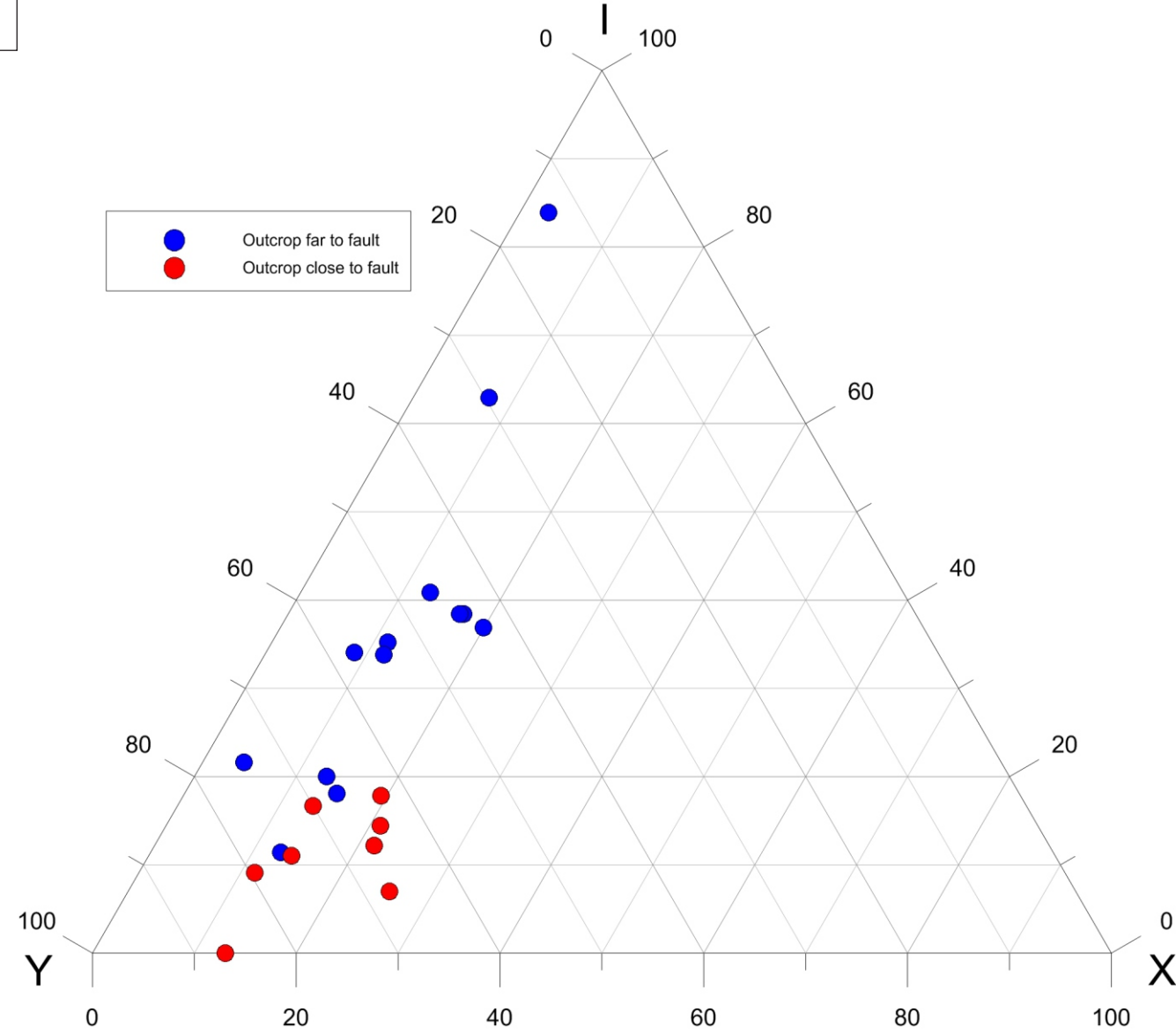
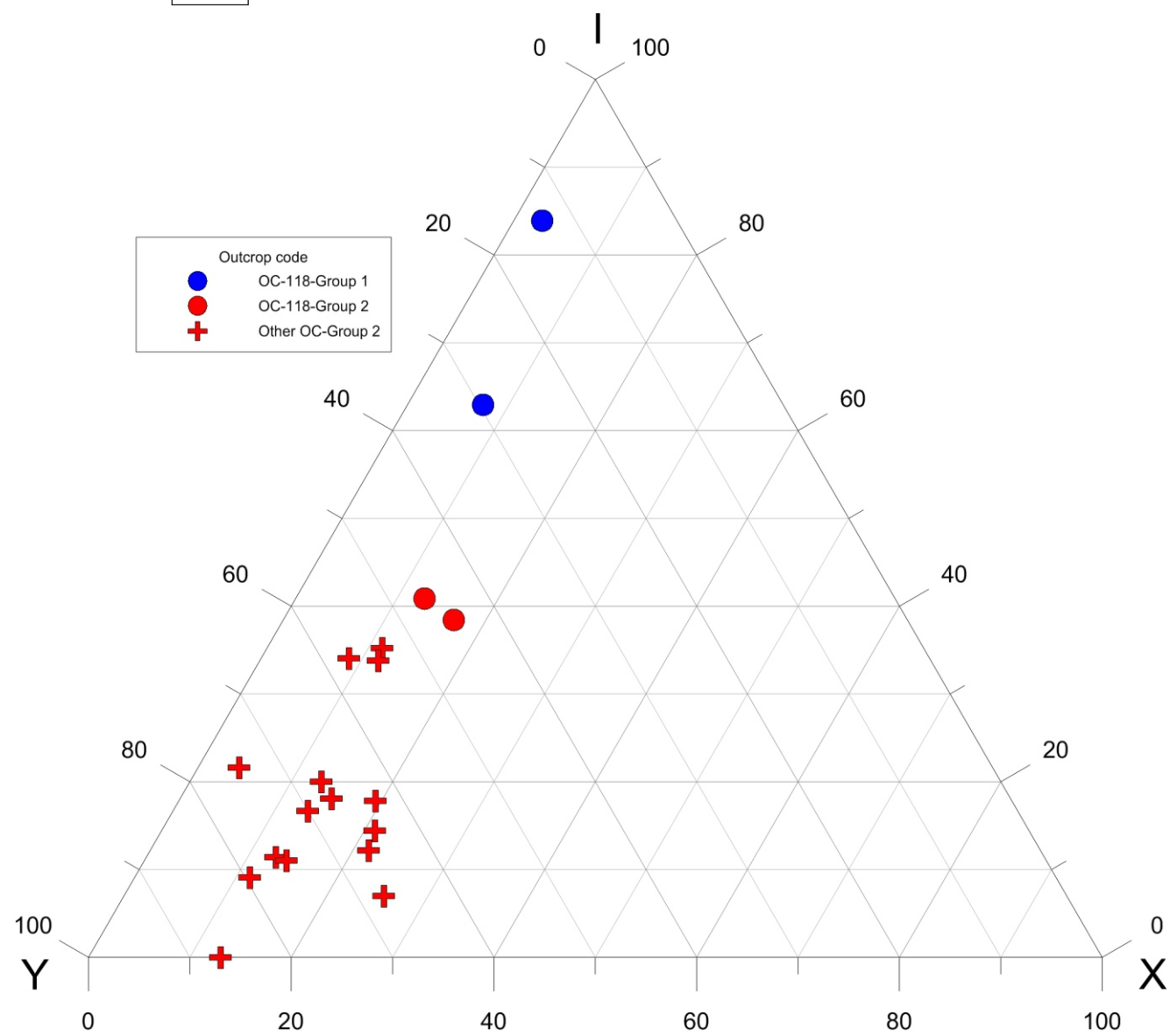




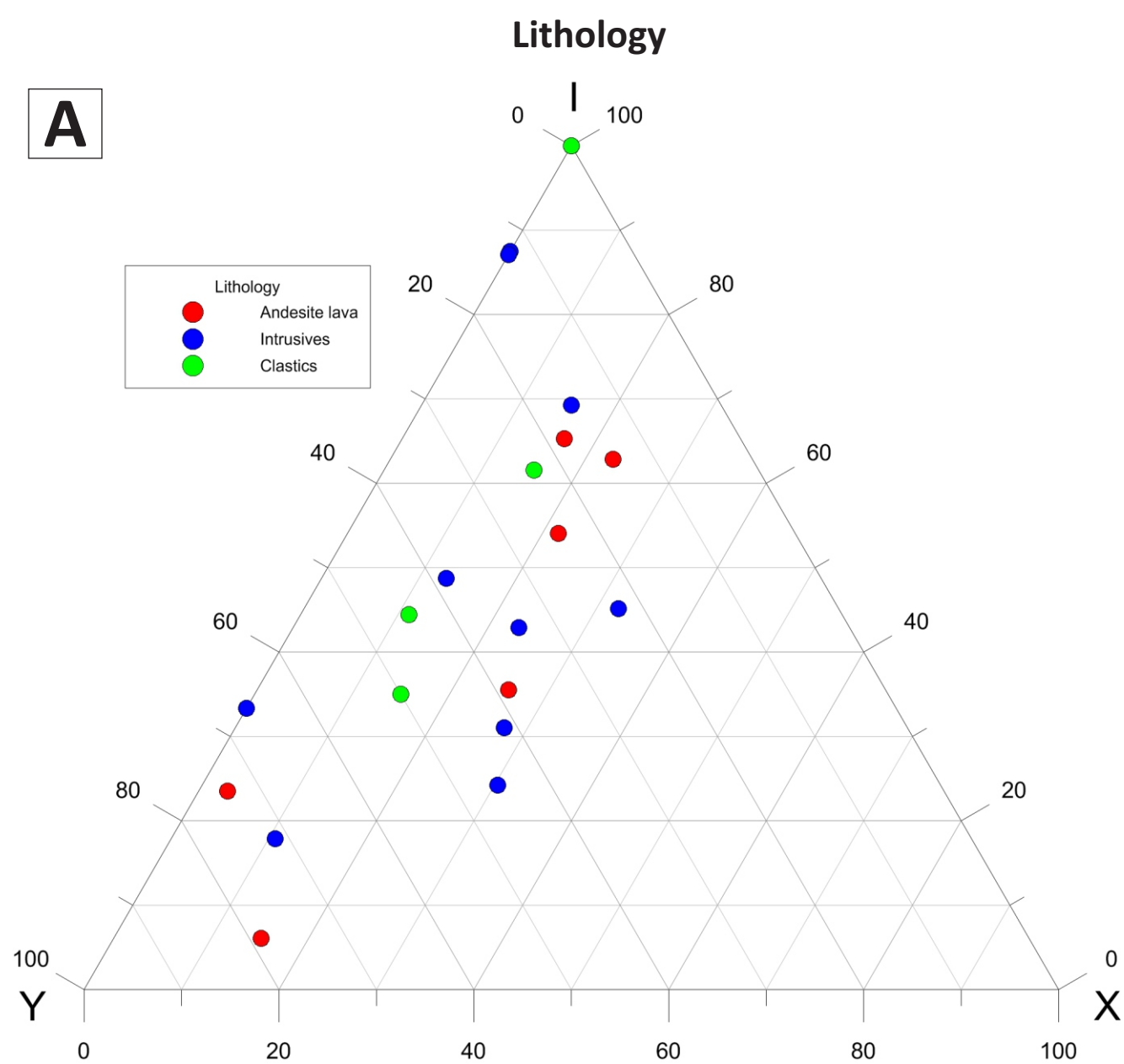




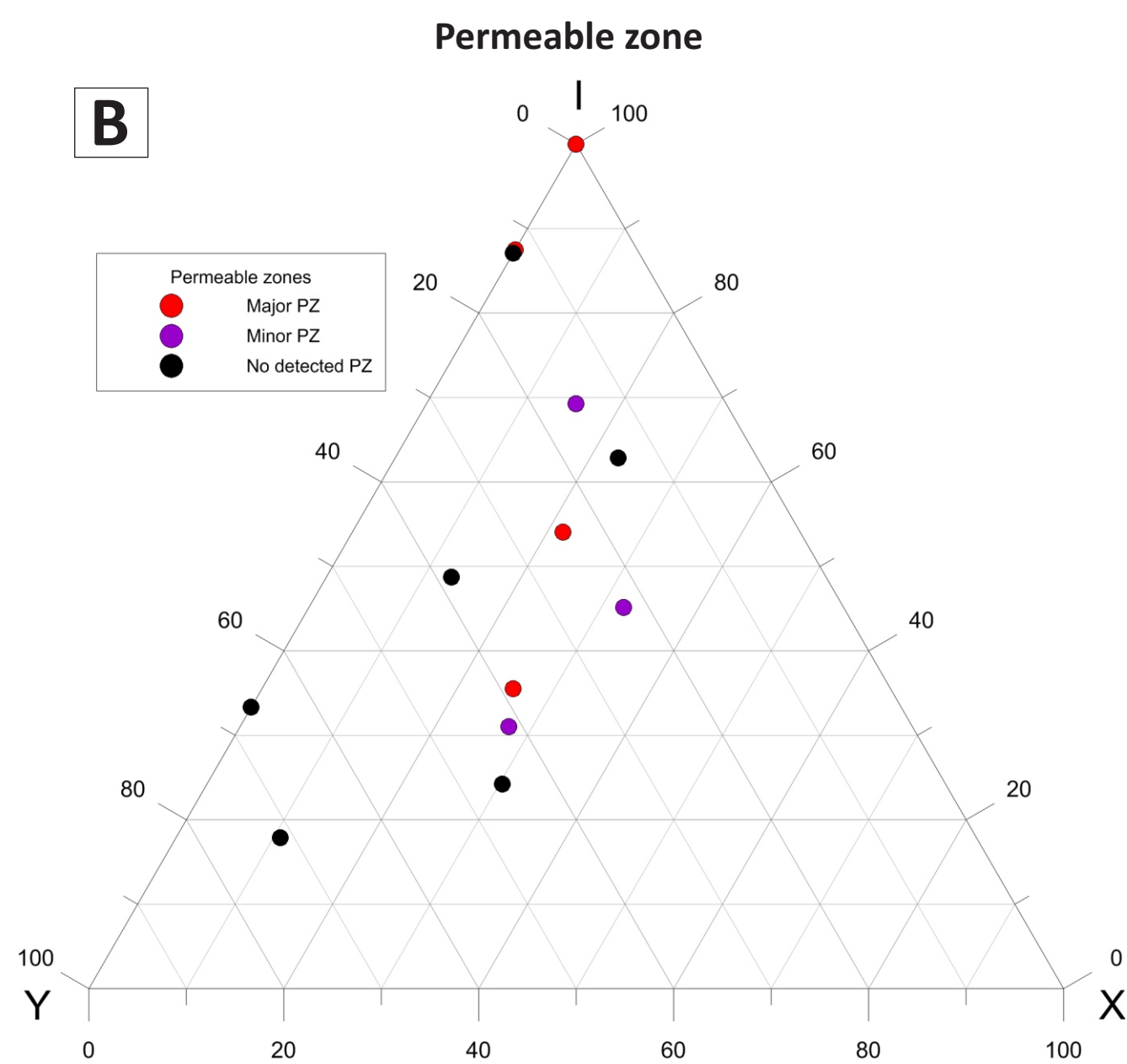


A**Evidence of alteration****B****Proximity to large faults****C****Fracture group**

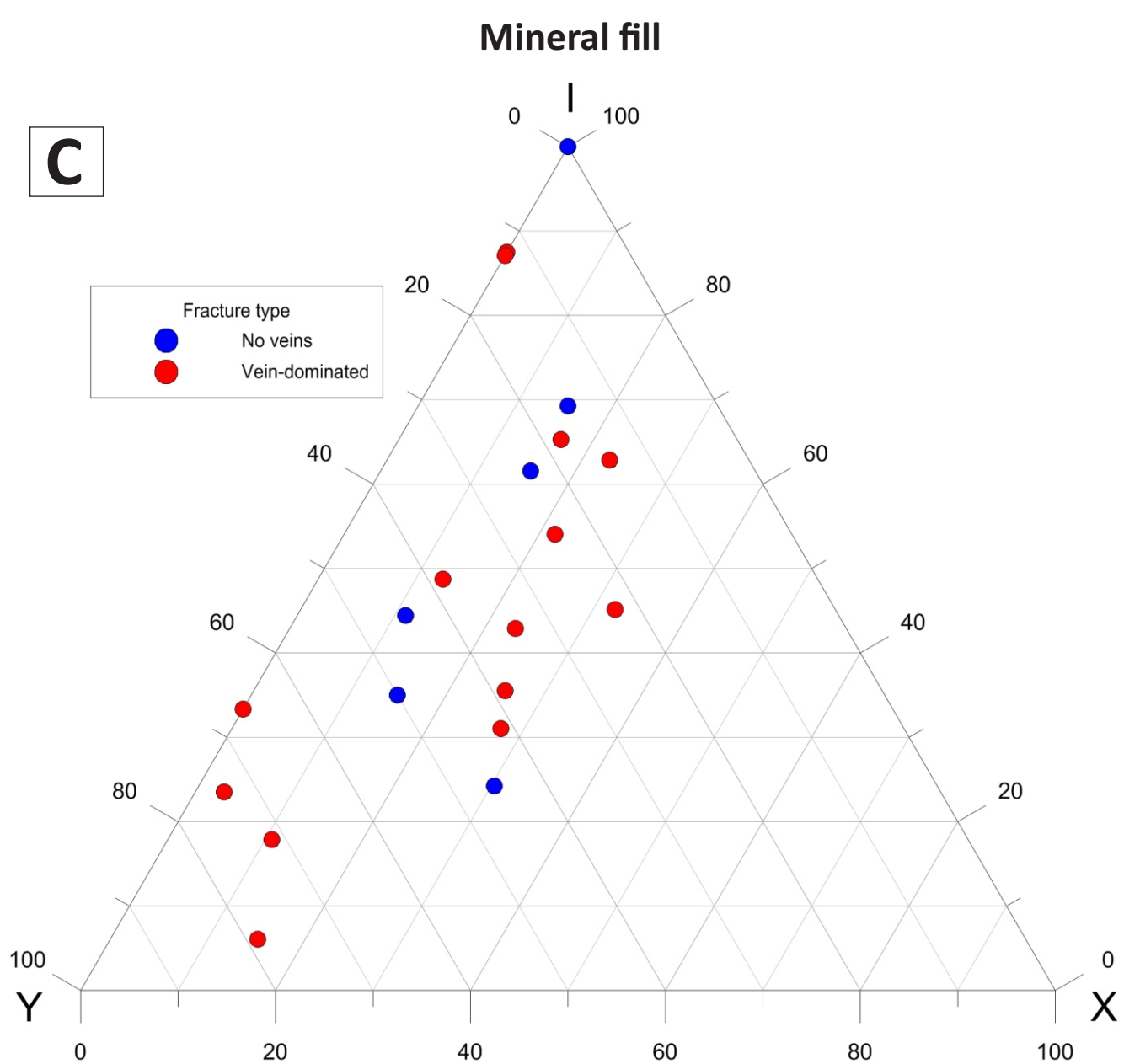
A



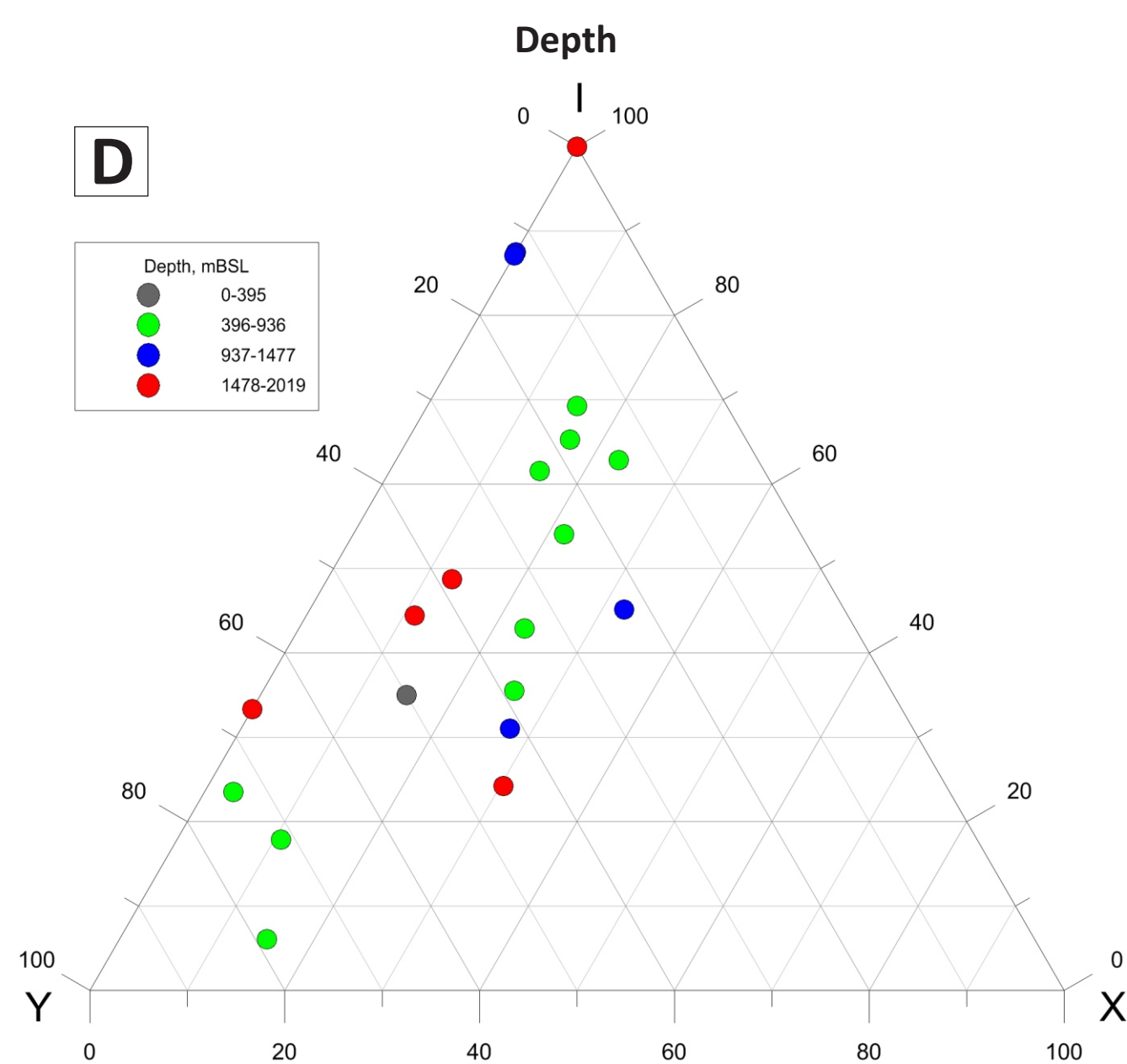
B

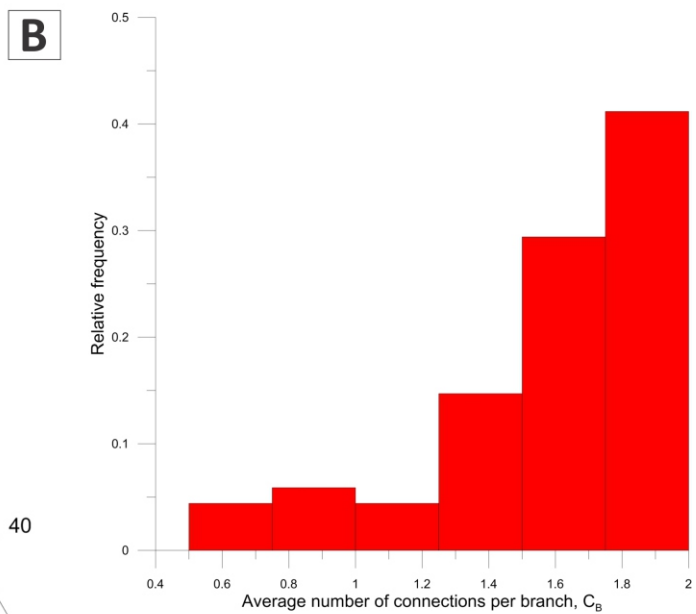
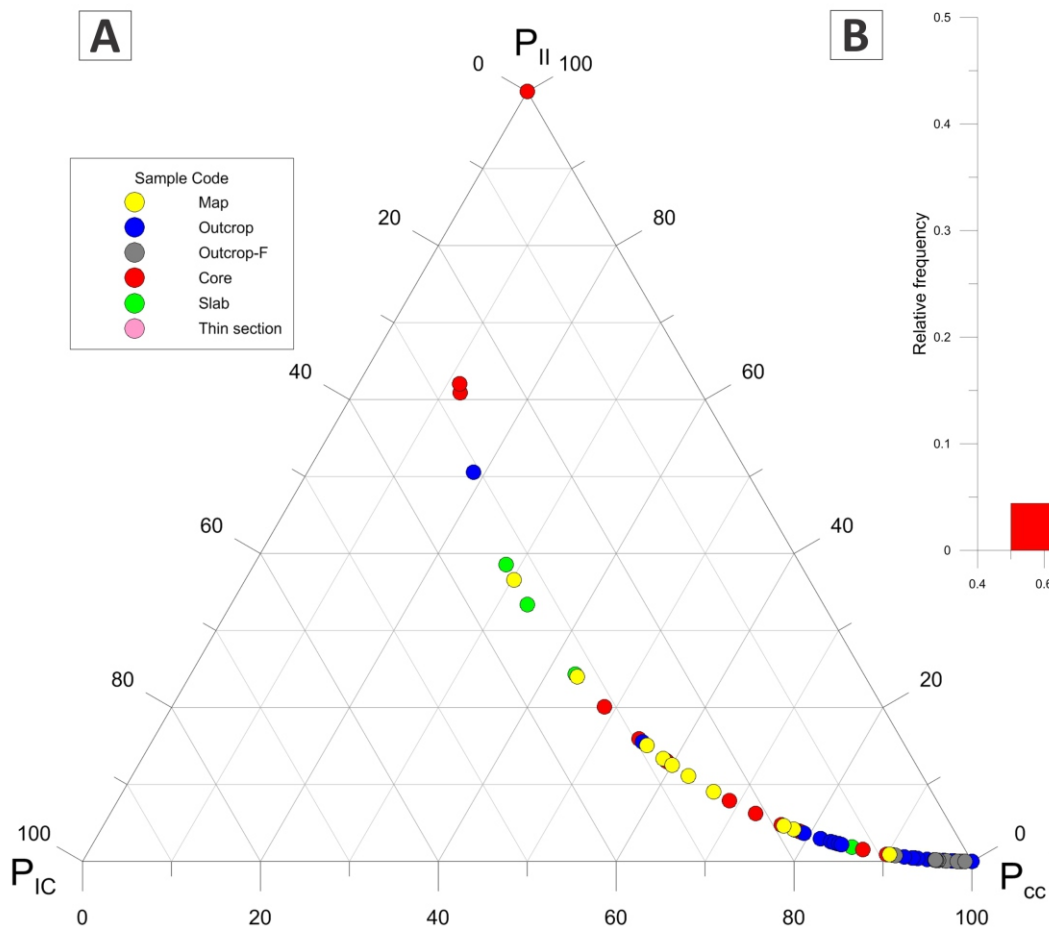


C



D





Supplementary material 1. Slopes, R2, and AIC values per distribution type of the cumulative frequency vs length plots of all fracture transects. R2 value highlighted in orange is the highest value, based on three significant figures; whilst the AIC in green is the lowest value for each dataset.

Scale		Transect Code	Normal			Log-normal			Exponential			Power		
			linear-linear			linear-log			log-linear			log-log		
			Slope	R2	AIC	Slope	R2	AIC	Slope	R2	AIC	Slope	R2	AIC
Regional		500K-NS	-3.00E-09	0.82	-3555	-7.00E-05	0.98	-393	-3.00E-05	0.94	-22	-0.77	0.97	-36
		500K-EW	-4.00E-09	0.61	-152	-8.00E-05	0.84	-160	-5.00E-05	0.86	7	-0.97	0.97	-9
		500K-NESW	-7.00E-09	0.97	-121	-6.00E-05	0.98	-123	-8.00E-05	0.99	-13	-0.71	0.92	-3
		500K-NWSE	-5.00E-09	0.97	-480	-1.00E-04	0.96	-469	-4.00E-05	0.96	-28	-0.94	0.82	8
		250K-NS	-3.00E-09	0.64	-391	-6.00E-05	0.9	-417	-9.00E-05	0.91	6	-1.55	0.99	-36
		250K-EW	-3.00E-08	0.65	-112	-3.00E-04	0.75	-115	-2.00E-04	0.86	6	-2.11	0.93	1
		250K-NESW	-1.00E-08	0.87	-91	-9.00E-05	0.92	-93	-9.00E-05	0.95	-4	-1.2	0.97	-7
		250K-NWSE	-1.00E-08	0.95	-352	-1.00E-04	0.98	-371	-9.00E-05	0.99	-54	-0.88	0.94	-20
		100K-NS	-4.00E-07	0.94	-338	-1.00E-03	0.98	-361	-4.00E-04	0.97	-41	-1.24	0.93	-24
		100K-EW	-2.00E-07	0.92	-222	-6.00E-04	0.98	-240	-5.00E-04	0.98	-32	-1.06	0.96	-20
		100K-NESW	-4.00E-07	0.94	-503	-9.00E-04	0.97	-529	-5.00E-04	0.97	-53	-1.14	0.88	-4
		100K-NWSE	-3.00E-07	0.92	-340	-8.00E-04	0.94	-344	-5.00E-04	0.92	-17	-1.17	0.85	-2
Sub-regional		50K-NS	-4.00E-07	0.88	-398	-1.00E-03	0.97	-440	-6.00E-04	0.97	-35	-1.71	0.93	-9
		50K-EW	-3.00E-07	0.94	-181	-6.00E-04	0.97	-188	-8.00E-04	0.97	-20	-1.37	0.94	-12
		50K-NESW	-4.00E-07	0.96	-342	-8.00E-04	0.99	-369	-6.00E-04	0.98	-47	-1.44	0.94	-23
		50K-NWSE	-6.00E-07	0.98	-344	-1.00E-03	0.98	-343	-9.00E-04	0.95	-29	-1.53	0.91	-17
		20K-NS	-6.00E-07	0.91	-356	-1.00E-03	0.97	-382	-9.00E-04	0.96	-22	-1.68	0.89	3
		20K-EW	-5.00E-07	0.93	-161	-1.00E-03	0.97	-170	-5.00E-04	0.96	-10	-1.37	0.93	-5
		20K-NESW	-6.00E-07	0.89	-317	-1.00E-03	0.96	-340	-7.00E-04	0.96	-34	-1.28	0.93	-19
		20K-NWSE	-6.00E-07	0.93	-336	-1.00E-03	0.98	-368	-7.00E-04	0.98	-39	-1.2	0.92	-10
Macroscale	Outside SNGF	OC-15	-0.74	0.79	28	-1.02	0.97	-78	-0.62	0.9	-36	-0.79	0.93	-61
		OC-17	-0.71	0.17	328	-4.47	0.85	234	-0.22	0.54	105	-0.81	0.97	-35
		OC-18	-1.18	0.79	66	-1.26	0.98	-28	-0.55	0.93	-49	-0.54	0.96	-75
	Inside SNGF	OC-74	-3.59	0.78	175	-2.42	0.99	10	-1.28	0.95	-53	-0.76	0.95	-43
		OC-81	-1.31	0.76	99	-1.19	0.99	-89	-0.75	0.91	-45	-0.61	0.95	-87

Mesoscale		OC-98	-10.4	0.76	163	-2.52	0.97	48	-3.11	0.94	-49	-0.68	0.98	-109
		OC-105	-0.14	0.81	-17	-0.54	0.97	-64	-0.25	0.95	-26	-0.89	0.98	-52
		OC-107	-10.57	0.71	282	-4.75	0.97	144	-1.68	0.89	-23	-0.68	0.97	-105
		W1-2	-1968.1	0.75	181	-54.08	0.96	150	-36.4	0.94	-12	-0.89	0.97	-29
		W1-3	-443.74	0.62	64	-31.58	0.75	61	-34.82	0.83	8	-2.35	0.9	3
		W2-2	-257.23	0.48	96	-14.63	0.86	80	-14.14	0.7	16	-0.7	0.94	-3
		W3-1	-742.38	0.86	189	-46.48	0.99	131	-9.92	0.97	-37	-0.56	0.92	-19
		W4-3	-211.58	0.88	81	-24.12	0.98	-16	-6.79	0.97	62	-0.72	0.94	-14
		W4-4	-284.1	0.87	58	-31.29	0.96	49	-6.92	0.96	-12	-0.73	0.98	-16
		W5-1	-2410.4	0.51	195	-90.59	0.86	174	-27.2	0.81	18	-0.87	0.99	-27
		W6-5	-2458.5	0.78	58	-39.12	0.93	49	-73.86	0.9	2	-1.11	0.97	-6
		W7-1	-638.42	0.7	117	-55.58	0.93	1	-8.74	0.88	99	-0.69	0.97	-15
		W7-3	-661.41	0.56	90	-18.57	0.87	76	-35.82	0.81	12	-0.84	0.88	7
		W8-5	-490.73	0.91	70	-22.81	0.98	54	-8.16	0.97	-23	-0.36	0.95	-17
		W9-3	-1593.9	0.55	195	-58.54	0.86	175	-2301	0.83	18	-0.73	0.96	-8

Supplementary material 2. Slopes, R2, and AIC values per distribution type of the cumulative frequency vs aperture plots of outcrop and well core fracture transects. R2 value highlighted in orange is the highest value, based on three significant figures; whilst the AIC in green is the lowest value for each dataset. Note that for OC-15, there is no clear trendline generated under a power law distribution (two trends with distinct slopes), hence, it was not included in the analysis.

Scale		Transect Code	Linear			Log-normal			Exponential			Power		
			linear-linear			linear-log			log-linear			log-log		
			Slope	R2	AIC	Slope	R2	AIC	Slope	R2	AIC	Slope	R2	AIC
Macroscale	Outside SNGF	OC-15	-0.01	0.22	-32.21	-0.22	0.91	-38.78	-0.02	0.56	-22.99	-0.13/ -1.41	0.96/ 0.93	0.32/ -37.7
		OC-17	-3.54	0.65	138.23	-3.52	0.98	48.86	-0.41	0.8	-8.02	-0.37	0.99	-85.1
		OC-18	-0.05	0.59	62.18	-0.56	0.94	6.72	-0.03	0.8	4.21	-0.29	0.97	-50.67
	Inside SNGF	OC-74	-0.7	0.61	106.14	-1.6	0.93	44.77	-0.41	0.88	7.91	-0.8	0.99	-65.43
		OC-81	-0.27	0.43	69.23	-0.54	0.9	8.15	-0.26	0.68	31.01	-0.43	0.99	-84.81
		OC-98	-1.07	0.52	78.23	-1.25	0.93	51.41	-0.58	0.8	25.68	-0.56	0.98	-16.11
		OC-105	-0.02	0.61	-2.3	-0.2	0.98	-71.29	-0.02	0.75	-2.24	-0.25	0.96	-44.22
		OC-107	-0.12	0.16	187.88	-2.2	0.78	141.67	-0.08	0.47	87.88	-0.71	0.97	-10.16
Mesoscale		W1-2	-8.66	0.3	187.82	-29.43	0.87	156.31	-0.28	0.59	34.22	-0.72	0.97	-18.5
		W1-3	-187.91	0.96	35.26	-12.68	0.89	42.76	-9.45	0.92	-0.86	-0.6	0.75	6.89
		W2-2	-3.04	0.89	13.15	-2.84	0.99	5.46	-0.57	0.97	-0.44	-0.53	1	-7.21
		W3-1	-18.8	0.23	144.26	-26.85	0.81	124.56	-0.63	0.56	30.3	-0.66	0.98	-12.59
		W4-3	-1.7	0.44	92.02	-8.25	0.75	83.21	-0.11	0.7	18.57	-0.44	0.91	5.41
		W4-4	-284.1	0.87	62.03	-31.29	0.96	59.2	-6.92	0.96	-8.76	-0.5	0.83	3.15
		W5-1	-27.13	0.68	94.28	-40.99	0.96	74.34	-0.41	0.83	2.36	-0.57	0.96	-12.3
		W6-5	-1111.4	0.76	89.22	-24.33	0.97	67.25	-3.11	0.92	-4.06	-0.62	0.97	-16.1
		W7-1	-638.42	0.7	89.57	-55.58	0.93	81.11	-8.74	0.88	18.53	-0.68	0.94	3.67
		W7-3	-66.61	0.72	76.88	-13.49	0.97	53.07	-2.65	0.87	2.2	-0.48	0.94	-5.33
		W8-5	-193.33	0.93	62.2	-24.99	0.97	53.33	-3.21	0.97	-20.94	-0.4	0.93	-12.29
		W9-3	-89.84	0.24	201.77	-60.35	0.76	181.5	-1.99	0.58	38.37	-0.97	0.96	-2.55